Measurement 224 (2024) 113943

Contents lists available at ScienceDirect

Measurement

journal homepage: www.elsevier.com/locate/measurement

Higher harmonics of the intensity modulated Photocurrent/Photovoltage spectroscopy response - a tool for studying photoelectrochemical nonlinearities

Adrian Olejnik [a,b,*], Katarzyna Grochowska [b]

[a] Department of Metrology and Optoelectronics, Faculty of Electronics, Telecommunications and Informatics, Gdańsk University of Technology, Narutowicza 11/12 St., 80-233 Gdańsk, Poland
[b] Centre for Plasma and Laser Engineering, Institute of Fluid-Flow Machinery, Polish Academy of Sciences, Fiszera 14 St., 80-231 Gdańsk, Poland

ARTICLE INFO

Keywords:
Intensity Modulated Photocurrent/ Photovoltage Spectroscopy
Harmonic analysis
Kinetic equations
Photoelectrochemistry
Photovoltaics

ABSTRACT

In this work, a higher harmonic analysis (HHA) of the intensity modulated photocurrent/photovoltage (IMPS/IMVS) spectroscopy data is proposed as a potent tool for studying nonlinear phenomena in photoelectrochemical and photovoltaic systems. Analytical solutions of kinetic equations were constructed for cases of single and double resonance accounting for various sources of higher harmonics. These sources correspond to the physical sources of nonlinear effects in the response including intensity-dependent generation current, intensity-dependent recombination, and second-order recombination. Due to the fact that the solutions for those cases are different, a qualitative methodology for analysis of harmonics is proposed. The methodology is illustrated by two experimental examples – Si photodiode for IMVS and TiO_2 nanotubes for IMPS. It was capable of distinguishing second order recombination in the first case and intensity-dependent transport rate for the latter.

1. Introduction

Semiconductor photoelectrochemistry is a research area that combines electrochemistry, solid-state physics/chemistry, surface chemistry and optics. In other words, it describes the chemistry and physics behind the reactions at the electrode/electrolyte interface induced by applied light irradiation. Historically, as the starting date of this interdisciplinary field one can assume 1839 when Edmond Becquerel demonstrated the photovoltaic effect. Nonetheless, the development of photoelectrochemistry can be rather dated back to the mid-20th century when its principles were established [1]. Anyway, it should be stated that photoelectrochemistry is strongly linked to the energy landscape and therefore its development has been dependent on the current trends in this area. Nowadays, the scientific word is more and more focused on innovative technologies and materials that can be used for applications in renewable energy, its conversion and storage as the widespread consumption of fossil fuels is causing not only the global warming and climate change but above all their depletion [2].

The primary features that should characterize new materials are high efficiency and long durability. Nonetheless, from the economic and environmental point of view the usage of eco-friendly components as well as mass production and cost effectiveness should be also taken into account [3]. Due to abovementioned reasons, high-efficiency crystalline silicon based solar cells such as e.g. tunnel oxide passivated contact solar cells [4], carrier selective contact solar cells [5] or silicon heterojunction solar cells [6], have attracted a lot of attention. Moreover, the works to reduce the costs of dye-sensitized solar cells to promote their commercialization are undertaken as this type of device is expected to meet requirements of the next generation [7]. One cannot also forget about the rapid development in the field of perovskite solar cells as they can become a game changer in the photovoltaic applications [8]. Apart from photovoltaic, another major topic of research is the application of photoactive materials in e.g. water splitting or CO_2 reduction [9]. Therefore, not only the new preparation methods or modifications of photoactive materials but also techniques to characterize their properties need to be developed.

Given the complexity of photoelectrochemical processes, the applied techniques should offer the information on such aspects as charge transport and recombination as well as the chemical reactions with different spatial and temporal resolution. Moreover, conventional characterization methods such as transmission electron microscopy, Raman spectroscopy and X-ray photoelectron spectroscopy allow only to

* Corresponding author.
E-mail address: aolejnik@imp.gda.pl (A. Olejnik).

https://doi.org/10.1016/j.measurement.2023.113943
Received 7 April 2023; Received in revised form 24 November 2023; Accepted 25 November 2023
Available online 25 November 2023

ex situ determination of the changes in samples morphology, crystal structure and chemical nature before and after testing. On the other hand, i*n situ* techniques can be used to establish information at applied voltage bias and during electrochemical reactions [10]. Among those techniques, scanning-photocurrent and scanning electrochemical microscopies allow to study the photovoltaic and catalytic properties of photoelectrodes, namely spatial photoactivity and spatial reaction kinetics. However, the most commonly employed technique is (photo) electrochemical impedance spectroscopy that is capable to capture carriers transport kinetics at the electrode/electrolyte interface [11].

Substantially different perspective on the same effects can be acquired by the intensity modulated photocurrent/photovoltage spectroscopies (IMPS/IMVS). These are versatile techniques for studying kinetics and mechanisms of the charge recombination, transport and transfer using light as a perturbation. In principle, they utilize the periodic modulation of the light intensity and measure the photocurrent/photovoltage response. Then, the frequency-dependent real and imaginary parts of the photocurrent/photovoltage are extracted through different integral transformations such as Fourier transforms. In most cases, a small perturbation limit is assumed per analogy with impedance spectroscopy methodologies to avoid nonlinear effects and preserve the linear response theory assumptions [12–14]. Commonly, several transfer functions Q(ω) and W(ω) - for IMPS and IMVS, respectively - are introduced and equivalent circuits (EC) are fit to the obtained data. As those objects – transfer functions and EC elements – are based on the linear response theory [15 16], they are meaningful only when the relation between light stimulus and photocurrent or photovoltage response of the sample is linear. Their main disadvantage, though, is the frequent inability to find a circuit that would represent the physical system, which may lead to doubtful interpretations of different elements. This problem was greatly magnified in recent studies involving IMPS microscopy [17]. However, relations between input and output signals can be strongly nonlinear for real samples rendering the linear approximation questionable. In electrochemical and photovoltaic systems (photo)current cannot be expressed as a linear function of the illumination flux or voltage even for simplest systems described by e.g., Shockley equation and Butler-Volmer equations - which are exponentials. Therefore, the typically used small perturbation approach (and EC) intrinsically limits the insight into the sample only to the two first terms in the Taylor series expansion. For such strongly (exponentially) nonlinear systems, the applied perturbation should approach zero to fulfil the linear approximation.

In several papers, a strong demand for high accuracy EC is emphasized in order to reflect physical quantities, e.g., for analysis of perovskite solar cells [14 17]. However, this requirement might unfortunately never be accomplished due to the intrinsic limitations of the equivalent circuit approach. That is because elements such as resistors, capacitors and Warburg elements are limited to the linear approximation. There are also several works with approaches other than the EC to interpret IMPS/IMVS experimental data and formulate theoretical predictions. These include solving the transport equation with different boundary conditions given for photoelectrons and holes, analytically [18–20] or numerically [17,21,22]. Although they greatly advance understanding of the intensity-modulated techniques and underlying photophysics, they rarely take nonlinear effects into account and have not provided a framework for their study so far.

In this work, an alternative perspective on the interpretation of the IMPS/IMVS data is presented, so that the treatment of the nonlinear effects is direct. The proposed approach involves spectral higher harmonic analysis (HHA) in addition to the fundamental AC response. According to the best knowledge of authors, it is reported for the first time for IMPS and IMVS. This perspective has been inspired by the nonlinear impedance theory that deals with nonlinear phenomena in 'dark' electrochemistry [23–26]. Firstly, a mathematical formalism of the HHA is developed for the IMPS and IMVS techniques based on solutions of the kinetic equations for several cases. Then, the formalism is applied to the study of experimental higher harmonic data obtained for two model systems: Si photodiode and loosely spaced titania nanotubes [27–30]. The purpose of this work is to create a new framework to treat nonlinear behaviors that are intrinsic to all the photovoltaic and photoelectrochemical systems to gain information that cannot be obtained solely from the fundamental (first) harmonic. The authors believe that the HHA formalism can be applied in a broader scope to solve the structural and functional puzzles of high efficiency perovskite solar cells [17] and photoactive metal organic frameworks [31]. For example, in the next sections it will be shown that the interpretation of 'negative resistances' and 'negative real parts in IMPS' [12,32,33] can be performed in the non-linear regime and can be easily captured by HHA.

2. Experimental

2.1. Preparation of electrodes

The Si photodiode was acquired from Instytut Fotonowy and measured without changes. Loosely spaced TiO_2 nanotubes were synthesized according to one of the protocols developed in our group. The data on chemical structure, morphology, electrical and optical properties of such nanotubes can be found in our numerous works [27–30]. Briefly, titanium foils (99.7 % pure) were anodized in the electrolyte containing 0.3 % NH_4F, 0.5 % HF, 7 % deionized water and diethylene glycol as the rest. Anodization was performed in the two-electrode system with Ti foil as anode and Pt mesh as a cathode in 40 ℃ temperature and 40 V for 2 h. Then the nanotubes were calcined at the tube furnace in 450 ℃ for 2 h to obtain crystalline, anatase phase. The samples area was equal to 0.785 cm^2 and the range of light illumination was between 0 and 1800 μW.

2.2. Methodology of IMPS/IMVS measurements and calculation of higher harmonics

IMPS/IMVS experiments were performed using devices provided by Instytut Fotonowy. Measurements were carried out in ambient temperature in either two or three electrode systems for Si photodiode and TiO_2 nanotubes, respectively. Information on the frequency ranges, applied potentials and magnitudes of the light intensity perturbation are given in each section separately. The real X(ω) and imaginary Y(ω) parts of all harmonics (including the fundamental) in the photocurrent response in IMPS are calculated as in-phase and quadrature components from **Equations (1–2):**

$$X(\omega) = \frac{\int_0^T j(t)\cos(n\omega t)dt}{T} \quad (1)$$

$$Y(\omega) = \frac{\int_0^T j(t)\sin(n\omega t)dt}{T} \quad (2)$$

where T is the period of applied oscillation, j(t) is current density, n is the number of harmonic and ω is a frequency. Analogous expressions were used to compute the real and imaginary parts of the photovoltage in the IMVS technique with the time function of the current density replaced by the corresponding time function of the voltage.

After obtaining the raw photocurrent I(t) or photovoltage U(t) time signal, the calculus (**Equations (1) and (2)**) is applied afterward on this signal to obtain real and imaginary parts of both the fundamental and higher harmonics. Details of the numerical integration and its software implementation are the intellectual property of the device provider – Instytut Fotonowy.

Experimental conditions for the IMVS and IMPS higher harmonics measurements are depicted in Scheme 1.

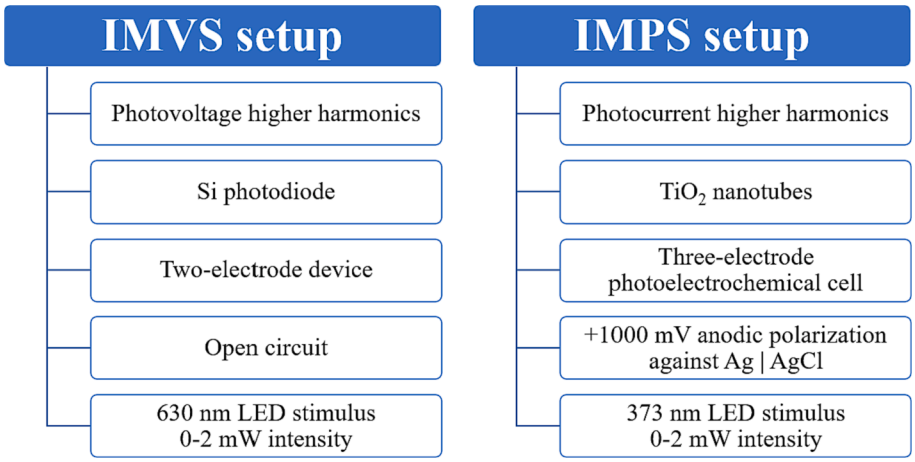

Scheme 1. Experimental conditions for the IMVS and IMPS higher harmonics measurements.

3. Theory

3.1. The concept of higher harmonics

It is an experimental fact that the photocurrent is not proportional to the illumination power density for most cases, especially when the relatively high magnitude of the light intensity stimulus is applied. Therefore, in the case of periodic light intensity input, the output current can be decomposed into a series of harmonics measured during the experiment:

$$j(t) = \sum_{n=0}^{\infty} j^{(n)} \exp(in\omega t) \tag{3}$$

here, $j^{(n)}$ is a frequency-dependent phasor of the n^{th} harmonic current having both real and imaginary part. Throughout the paper, the small letter "j" is used as a symbol of current, because the small "i" and large "I" letters are used in other contexts. Phasor notation is understood in the following way:

$$j^{(n)} = j^{(n)}_{amplitude} \exp(i\varphi_n) \tag{4}$$

The phasor consists of the amplitude component and the phase shift component. In general, each phasor can be different for each harmonic - for n = 1 it is equivalent to standard analyses of the fundamental frequency. In other words, every harmonic has its own real and imaginary part with a unique frequency dependence and the corresponding Bode and Nyquist plots. In the following section, mathematical models are developed to interpret several measured harmonic phasors. It is to be noted that the real signals always comprise of both positive and negative frequencies. In this part, only positive complex exponentials are assumed as the stimulus for simplicity. However, in the Supporting Information (SI) file, a discussion on the case for both positive and negative exponentials is provided. It is illustrated that higher harmonics can couple with the fundamental leading to the interpretative danger when using solely first harmonic analysis (Section 1. Equations s1 - s5, ESI file).

3.2. Transport equation and intensity-dependent generation current

In general, to obtain analytical expressions for higher harmonics, one should solve the full version of a diffusion-recombination-generation type of the transport problem written for photogenerated charge carriers:

$$\frac{\partial Q}{\partial t} = D\frac{\partial^2 Q}{\partial x^2} - k_R Q + J_{gen}(t)\alpha\exp(-\alpha x) \tag{5}$$

where Q is electron charge density (in SI units: C/m^3), D is diffusion constant (m^2/s), k_R is a recombination rate (1/s), J_{gen} is a time-dependent generation current density (A/m^2), and α is the optical absorption coefficient (1/m). This equation was recently solved analytically in the context of IMPS/IMVS applied to perovskite solar cells in works [18–20] using the Laplace transform. There are also several works attempting to solve the problem numerically using kinetic perspective [17,21] or EC perspective [13]. In both approaches, only the fundamental harmonic response was considered so far. The spatial dependence of the generation current is typically given by the Lamber-Beer expression [19,34,35] and its time dependence as the Gartner equation [20,36]. It states a linear dependence on the light power density and is still frequently used in the literature [37,38]:

$$J_{gen}(t) = J^0(1 + \exp(i\omega t)) \tag{6}$$

Experimental observations reveal that this assumption is generally not true, which was already known in 1990 [36]. Besides the nonideality of the charge collection validating this approximation, there are saturation effects that manifest especially when using high illumination intensities (see Fig. 5**a** for saturation of the voltage in photodiode and Fig. 8**c** for saturation of the current in the TiO_2 sample). Therefore, a more accurate description would be to abandon the linear approximation and express the generation current, e.g., as the following Taylor expansion:

$$J_{gen} = f(\Phi) = \sum_{n=0}^{\infty} a_n \left(\frac{\Phi}{\Phi_0}\right)^n \tag{7}$$

where Φ is the power density, Φ_0 is a constant – authors give it a name of the limiting power density - and a_n are polynomial coefficients with physical units of current. Limiting power density is introduced for dimensional purposes. Its physical meaning would be such a high power density that the generation current is constant and no longer depends on the power density. Coefficients a_n contain information on the generation current dependence on the light intensity and should reflect the saturation effect. The convergence of this series and all series developed further in the formalism is discussed in the **ESI file** in Section 2. If a periodic stimulus with DC and AC components is applied to the sample having the form:

$$\Phi(t) = \Phi_{DC} + \Phi_{AC}\exp(i\omega t) \tag{8}$$

the sample with non-linear generation will produce the generation photocurrent expressible as a series of harmonics:

$$J_{gen}(t) = \sum_{n=0}^{\infty} a_n \left(\frac{\Phi_{DC} + \Phi_{AC}\exp(i\omega t)}{\Phi_0}\right)^n = \sum_{n=0}^{\infty} J^{(n)}\exp(i\omega n t) \tag{9}$$

here $J^{(n)}$ are frequency-independent phasors of the generation current obtained by contracting all the terms in the infinite series. These quantities can be extracted from measurements of the higher harmonic spectra of the photovoltage or photocurrent. Such generation current is plugged into the transport equation (5), which will be solved in the simplified form. Let's assume that the Laplacian of charge density is constant at x = 0 (but still time dependent).

This approximation allows to transfer the partial differential equation transport problem to the ordinary differential equation (Discussion of the mathematical technicalities of this approximation can be found in E**SI** in Section 3.):

$$\frac{dQ}{dt} = Const. - k_R Q + J_{gen}(t)\alpha \tag{10}$$

A redefinition of the generation current from J_{gen} to I_{gen} by absorbing the optical absorptivity α and constant resulting from the constant Laplacian approximation can be done:

$$J_{gen}(t)\alpha + Const. = I_{gen}(t) - j_{ext}(t) \tag{11}$$

where the initial unit of J_{gen} was A/m^2 and I_{gen} is now A/m^3. This redefinition leads to the set of well-known kinetic equations having the form:

$$\frac{dQ}{dt} = I_{gen}(t) - k_R Q - j_{ext}(t) \tag{12}$$

It is to be noticed that this form is invariant to the current and charge dimensions because spatial dimensions cancel out. The unit of Q can be either C (total charge), C/m^2 (surface charge density), or C/m^3 (bulk charge density) and the corresponding photocurrent j_{ext} or generation current I_{gen} are A (total current), A/m^2 (surface current density), or A/m^3 (bulk current density).

In the case of IMVS boundary conditions, the circuit is open and $j_{ext} = 0$. In the case of IMPS, **Equation (12)** was extensively studied, e.g. by LM Peter and Ponomarev with different complexity of models [39–41]. Although this picture has its limitations, it has several advantages over the equivalent circuits approach. The most important one is the possibility of direct physical interpretation of quantities such as recombination rate, charge transfer rate without referencing to the EC perspective. In terms of circuit elements, these can be associated with resistances and capacitances [42–46], e.g.:

$$k_R^x = \frac{1}{R_{rec}^x C_\mu^x} \tag{13}$$

$$k_{CT} = \frac{1}{R_{CT} C_H} \tag{14}$$

where R_{rec}^x and C_μ^x are recombination resistance and chemical capacitance, R_{CT} and C_H are charge transfer resistance and Helmholtz capacitance. X stands for different possible mechanisms of recombination e.g. bulk recombination, trap-assisted recombination, surface state recombination [44], etc. In the standard analysis using only the fundamental harmonic, each type of recombination can be associated with its own recombination resistance and chemical capacitance.

However, in the picture proposed in this work there is no necessity for interpretation of rates as the circuit elements, which leads to the possibility of analyzing higher harmonic response. In the next section, it will be shown that when rate constants (or generation current) are made intensity-dependent, their interpretation as resistances and capacitances becomes vague. Solutions for such models including both fundamental and higher harmonics of the IMPS and IMVS response will be presented for several cases:

1) Single resonance: Intensity-independent generation current
2) Single resonance: Intensity-dependent recombination rate
3) Single resonance: Second order recombination
4) Two resonances: Intensity-independent generation current

4. Solutions of kinetic equations with higher harmonics

In the most simple model, the semiconductor can be viewed as a black box for generation, separation and transport of carriers after light illumination. In this case, a single kinetic equation is written for the whole system and, for most cases, single resonance is produced. It could be visually thought as all the regions e.g. space-charge region, quasi-neutral region, surface state "lumped together" as a single entity. It is true that this crude approach does not account for many parallel phenomena because typically there are 2–4 resonances for the cell or device. However, it is a useful playground to introduce various mechanisms for generation of higher harmonics with minimally complicated equations.

4.1. Single resonance: Intensity-dependent generation current

Equation (15) describes a single resonance problem in IMPS. Mathematically simplest way of introducing higher harmonics into the response is making the generation current intensity dependent per analogy to the **Equation (9)**:

$$I_{gen}(t) = \sum_{n=0}^{\infty} I^{(n)} \exp(i\omega n t) \tag{15}$$

As a result, the solution for charge density also becomes a series of harmonics:

$$Q(t) = \sum_{n=0}^{\infty} Q^{(n)} \exp(i\omega n t) \tag{16}$$

The measurable photocurrent has also the same form:

$$j_{ext}(t) = \sum_{n=0}^{\infty} j^{(n)} \exp(i\omega n t) \tag{17}$$

Which can be connected to the charge by the relation:

$$j_{ext}(t) = k_{tr} Q = \frac{Q}{RC} \tag{18}$$

where k_{tr} is a transport rate related to resistance R and capacitance C in a very general sense. In real devices and photoelectrochemical cells R would be composed of series resistance, shunt resistance, and all resistances of the semiconductor itself [47]. Similarly, C is a composition of geometrical capacitance, chemical capacitances and other charge storage mechanisms. In particular, when diffusion (concentration field gradient) is a dominating way of transport, R and C can be associated with diffusion resistance and capacitance. Then, diffusion constant could be estimated as $D = L^2 k_{tr}$, where L is characteristic diffusion length. On the other hand, when the migration (electric potential gradient) is dominant, R and C could be associated with injection resistance and capacitance [48 49], and carrier mobility could be resolved. In fact, it is irrelevant which resistances and capacitances dominate in which case for the discussion of the IMPS/IMVS higher harmonics because the mathematics is the same for any type of resistance or capacitance. Other phenomena (and associated resistances and capacitances) such as charge transfer rate, trapping and detrapping, etc. could be analyzed analogously as separate resonances and the structure of solution for higher harmonics would be similar (for each resonance). Nevertheless, the solution for the intensity-dependent generation problem can be approached by plugging complex exponentials as follows:

$$i\omega n \sum_{n=0}^{\infty} Q^{(n)} \exp(i\omega n t) = \sum_{n=0}^{\infty} I^{(n)} \exp(i\omega n t) - k_R \sum_{n=0}^{\infty} Q^{(n)} \exp(i\omega n t) - k_{tr} \sum_{n=0}^{\infty} Q^{(n)} \exp(i\omega n t) \tag{19}$$

The solution for $Q^{(n)}$ is a set of n algebraic equations - each one per each harmonic. In this case, it is possible to get analytical expression for all harmonics at once by comparing coefficient of each exponent. The result is the frequency-dependence of the charge density reflecting the shape of real and imaginary part of IMPS harmonics:

$$i\omega n Q^{(n)} = I^{(n)} - (k_R + k_{tr})Q^{(n)} \tag{20}$$

After rearrangement and decomposition to the real and imaginary parts:

$$Q^{(n)} = \frac{I^{(n)}}{i\omega n + k_R + k_{tr}} = \frac{I^{(n)}(k_R + k_{tr})}{(n\omega)^2 + (k_R + k_{tr})^2} - i\frac{n\omega I^{(n)}}{(n\omega)^2 + (k_R + k_{tr})^2} \tag{21}$$

According to the proportionality in the **Equation (18),** the measurable n-th harmonic of the photocurrent is just a rescaled n-th harmonic of the $Q^{(n)}$. Corresponding IMPS plots are shown in Fig. 1a–c.The real part has maximum at the frequency equal to zero and decays monotonously to zero until the infinite-frequency limit. The imaginary part has a maximum at the frequency equal to $k_R + k_{tr}$ and also decays to zero at high frequency limit. For the first harmonic (n = 1), this behavior corresponds to the single semicircle (single resonance) on the Nyquist plot, with the points approaching the complex plane origin in the high – frequency limit. In this model, higher harmonics $Q^{(n)}$ exhibit exactly the same shape of the real and imaginary parts, but the frequency of the resonance (and the maximum of the imaginary part) is shifted to lower values according to the harmonic number n:

$$\omega_{IMPS}(n) = \frac{k_R + k_{tr}}{n} \tag{22}$$

Moreover, amplitudes of harmonics vary according to the Taylor coefficient of the generation current $I^{(n)}$, which capture the intensity-dependence of the generation.

Analogous solution for the IMVS can be obtained by assuming external current equal to zero. The resulting charge density will be:

$$Q^{(n)} = \frac{I^{(n)}}{i\omega n + k_R} = \frac{I^{(n)}k_R}{(n\omega)^2 + (k_R)^2} - i\frac{n\omega I^{(n)}}{(n\omega)^2 + (k_R)^2} \tag{23}$$

In the single resonance cases, a proportionality between the n-th harmonic of the charge density and the n-th harmonic of the measurable photovoltage can be established as Q = UC. Therefore, IMVS solution is a single resonance with the maximum of the imaginary part centered at (see Fig. 1d–f):

$$\omega_{IMVS}(n) = \frac{k_R}{n} \tag{24}$$

Overall, by making the generation current intensity-dependent, higher harmonics of the IMPS and IMVS emerged. In this model, every harmonic has the same shape but differs with the resonance position and the amplitude. In the next subsections, another ways of introducing the higher harmonics are presented.

4.2. Single resonance: Intensity-dependent recombination rate

When the light intensity is high enough for the higher harmonics to appear, the assumption of constant recombination rate may no longer valid. In several works, it was stated that increasing power density leads to increased transport rate [50–52]. Although not fully understood for a broad class of materials, this is a generally repeating trend for metal oxide semiconductors. In the case of recombination rate, its dependence on the light intensity is not as straightforward, and there is a limited amount of work to draw conclusions. In the paper of Xiao et al. it was shown through the IMVS technique that the recombination rate increases almost linearly with power density Φ in TiO_2-based junctions [50]. In other studies, with the photoimpedance spectroscopy an analogous trend has been presented on hematite electrodes [53,54]. On the other hand, Spera et al. have recently shown that for $CuInS_2$ - based photovoltaic cells, the shape of its dependence varies with the wavelength of the illumination – for 635 nm there is a similar increasing trend and for 450 nm there is a maximum at some value of power density [22,55] and then decay. The physical origin of the recombination increase could be associated with either the lower separation capability due to the lower electric field in the space-charge region during high illumination, or the higher collision probability of photogenerated carriers – thus annihilation.

Regardless of the causes of the intensity dependence, one could write its Taylor-like expansion in the way it was performed for the generation current in **Equation (15)**. In case of the periodic light stimulus, it would be equal to the series:

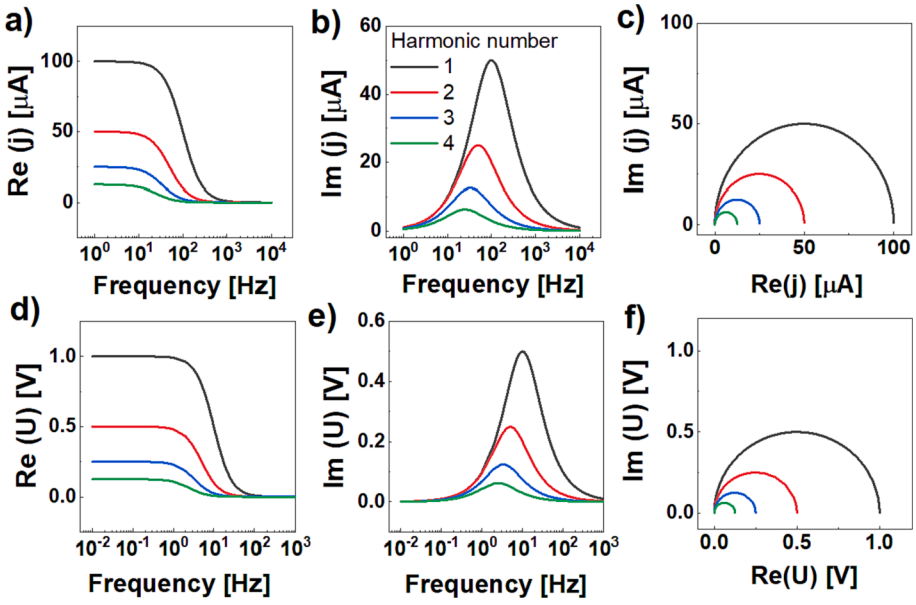

Fig. 1. Higher harmonic solutions for the intensity-dependent generation model; a-c) real, imaginary and Nyquist projections for the IMPS; d-f) real, imaginary and Nyquist projections for the IMVS. Constants used for construction of plots: k_R = 10 Hz, k_{tr} = 100 Hz, $I^{(0)} = I^{(1)}$ = 100 μA, $I^{(2)}$ = 50 μA, $I^{(3)}$ = 25 μA, $I^{(4)}$ = 12.5 μA, R = 10 kΩ, C = 10 μF.

$$k_R(\phi(t)) = \sum_{n=0}^{\infty} b_n \left(\frac{\Phi}{\Phi_0}\right)^n = \sum_{n=0}^{\infty} {k_R}^{(n)} \exp(i\omega n t) \tag{25}$$

where b_n and Φ_0 are defined analogously as in **Equation (9)** and $k_R^{(n)}$ are higher harmonic components for the recombination rate. Other rates including transport rate k_{tr} or charge-transfer rate k_{CT} can be made intensity-dependent in analogous way if necessary. The single-resonance problem for the intensity-dependent recombination rate has the following solutions for higher harmonics of the charge density (full derivation is available in ESI file in Section 4:

$$Q^{(1)} = \frac{I^{(1)} - k_R^{(1)} Q^{(0)}}{i\omega + k_R^{(0)}} \tag{26}$$

The first harmonic consists of a single resonance with one characteristic frequency $\omega = k_R^{(0)}$.

$$Q^{(2)} = \frac{A}{2i\omega + k_R^{(0)}} + \frac{B}{i\omega + k_R^{(0)}} \tag{27}$$

Due to the intensity-dependence of the recombination constant the second harmonic is no longer a single Lorentzian, but a sum of two Lorentzians. A and B are constants composed of Taylor coefficients of intensity-dependent recombination and intensity-dependent generation (see Section 4 in **ESI** for details). Those constants can be interpreted as weighting factors for two resonances. The first one has the maximum of the imaginary part centered at exactly $\omega = k_R^{(0)}$, but the second one is centered at $\omega = k_R^{(0)}/2$. Finally, the general expression for n-th harmonic in the intensity-dependent recombination rate model is the following:

$$Q^{(n)} = \sum_{m=1}^{n} \frac{A^m}{i\omega m + k_R^{(0)}} \tag{28}$$

where $A^{(n)}$ is some constant depending only on Taylor coefficients $k_R^{(n)}$ and $I^{(n)}$, although in a complicated way. There is always a sum of n Lorentzians with either maxima or minima superimposed onto single line. Depending on the value of the Taylor coefficients (which reflect the shape of intensity-dependence for the generation and recombination) maxima on the imaginary part can be positive or negative [12]. For the second harmonic the situation is depicted in Fig. 2.

In the case of the second harmonic, even if the nonlinear generation term $I^{(2)}$ is zero, the number of imaginary part maxima for the second harmonic is still two (**Equation S17-19** is Section 4). However, if the $k_R^{(1)}$ coefficient is set to zero (effectively making recombination intensity-independent) the number of maxima is reduced to one – exactly as in the intensity-dependent generation model. Therefore, it is the intensity dependence of the recombination constant solely that can cause emergence of several new (apparent) characteristic time constants. Characteristic frequencies are lower than the fundamental and amplitude of each is dependent on the values of Taylor coefficients. Thus, the number of maxima on the imaginary part of higher harmonics can serve as a qualitative diagnostic tool for distinguishing of intensity-dependent generation versus intensity-dependent recombination.

It is to be noted that the solution for intensity-dependent transport and charge transfer in IMPS has exactly the same structure. The only difference is the rates k_{tr} or k_{CT} would be made intensity-dependent according to the **Equation (25)** instead of the recombination rate. They can be altogether made intensity-dependent as well, and the solution for higher harmonics would still be the same as **Equation (28)** with A^n constant being even more complicated.

It is also redundant to distinguish between intensity-dependent rate (e.g., recombination rate) and intensity-dependent resistances or capacitances associated with this rate. Solutions for higher harmonics are mathematically equivalent (see Sections 5–7 in **ESI**). There are of course, series and shunt resistance, although they do not depend on the light intensity, therefore are not expected to generate IMPS/IMVS higher harmonic responses.

The presence of negative real and imaginary parts observed in perovskite solar cells [32] might be a nonlinear effect resulting from the intensity-dependent recombination/transport rate. Such an outcome might not originate from instrument limitations, but the fact that the

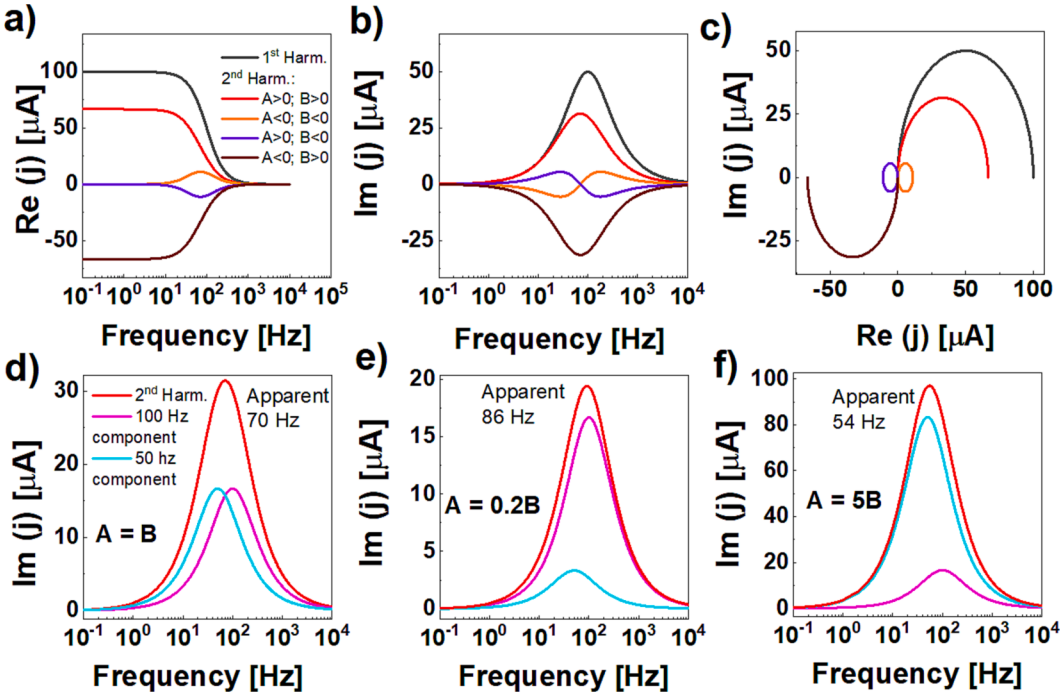

Fig. 2. Spectra of the first and second harmonics of IMPS simulated for the model of the intensity-dependent recombination model. Real (a), imaginary (b) and Nyquist (c) plots for: A > 0 and B > 0; A > 0 and B < 0; A < 0 and B > 0; A < 0 and B < 0; d-f) deconvoluted imaginary parts for A > 0 and B > 0 with various proportions illustrating variable apparent characteristic frequency for the same contributing resonances. Constants are equal to: $k_R^{(0)} = 10$ Hz, $k_{tr} = 100$ Hz, $I^{(0)} = I^{(1)} = 100$ μA, $I^{(2)} = 50$ μA, R = 10 kΩ, C = 10 μF.

instrument forces the linear approximation and ignores the signal of higher harmonics. Of course, there is another possible explanation of the negative real parts in the cited works i.e., the negative slope on the light intensity dependence of the photocurrent(photovoltage) [33].

4.3. Single resonance: Second order recombination

Besides making the quantities intensity-dependent, another way of introducing the nonlinearity and higher harmonics into IMPS is making the recombination second (or higher) order. This type of recombination is expected to be dominant in many types of photovoltaic cells, including perovskites [56]. The kinetic equation for this case is the following:

$$\frac{dQ}{dt} = I_{gen}(t) - kQ - \Psi Q^2 \tag{29}$$

where k is the first-order and Ψ is the second-order recombination rate – for simplicity they are intensity-independent in this model and the external current is dropped again. However, higher harmonics will still be resolved. It is to be noted that recombination is annihilation of the free electron with a hole, thus the electron density should multiply hole density. However, analogous equation can be derived for holes - this view was adopted in related works [57 58].

Solution for the first harmonic of the second order recombination problem is the fully analogous to the previous models (see Section 8 in ESI for the full derivation):

$$Q^{(1)} = \frac{I^{(1)}}{i\omega + k'} \tag{30}$$

For the IMVS case the reduced constant k' installed into **Equation (30)** will be equal to $k' = k + 2\Psi Q^{(0)}$, and for IMPS $k' = k + k_{tr} + 2\Psi Q^{(0)}$. After decomposition to simple fractions, the second harmonic can be expressed as:

$$Q^{(2)} = \frac{A}{2i\omega + k'} + \frac{B}{i\omega + k'} + \frac{E}{(i\omega + k')^2} \tag{31}$$

where A, B and E are frequency-independent constants resolvable from the simple fraction decomposition (Equation (s44) in Section 8 of the ESI). If E was equal to zero, the result would be exactly the same as in the intensity-dependent recombination model. However, due to the square in the denominator, the last term introduces completely different behavior. The real part has now a minimum located at $\omega = k'\sqrt{3}$. The imaginary part has also a single maximum, but it is located at $\omega = k'/\sqrt{3}$.(Fig. 3)

As a result, the solution for the second order recombination is qualitatively different for two previous models – the presence of these functions can only be obtained for the second (or higher) order process such as recombination. Existence of the real part extrema on the second harmonics could be considered as additional mark of the second (or higher) order recombination. It is to be noted that in principle other processes such as trapping/detrapping can be second order. Solutions for those processes will be exactly the same as for the second order recombination – the only change would be the meaning of the Ψ and other constants.

4.4. Two resonances: Intensity-dependent generation current

After deriving equations for the single resonance, it is worthy to apply the acquired concepts and associated intuition for a model of two resonances. This view corresponds to the division of the system into several parts such as the space-charge region, Helmholtz layer, surface state area. Each region can have its own kinetic equation and IMPS/IMVS higher harmonics can be introduced in every way discussed in the previous section. Additional effects such as trapping/detrapping and distinguishing several types of recombination can be also included analogously.

Example of the two-resonance model for the fundamental harmonic can be found in both older and newer literature. In the seminal paper of Peter and Ponomarev, the case of two resonances was modelled in the following way [39]:

$$\begin{cases} \dfrac{dQ_{SC}}{dt} = I_{gen} - k_R(Q_{SC} - Q_H) - j(t) \\ \dfrac{dQ_H}{dt} = k_{CT}(Q_{SC} - Q_H) - j(t) \\ \dfrac{Q_{SC}}{C_{SC}} + \dfrac{Q_H}{C_H} = jR \end{cases} \tag{32}$$

where the first equation quantifies the Q_{SC} charge flow in the space charge layer with I_{gen} being generation current, k_R recombination rate

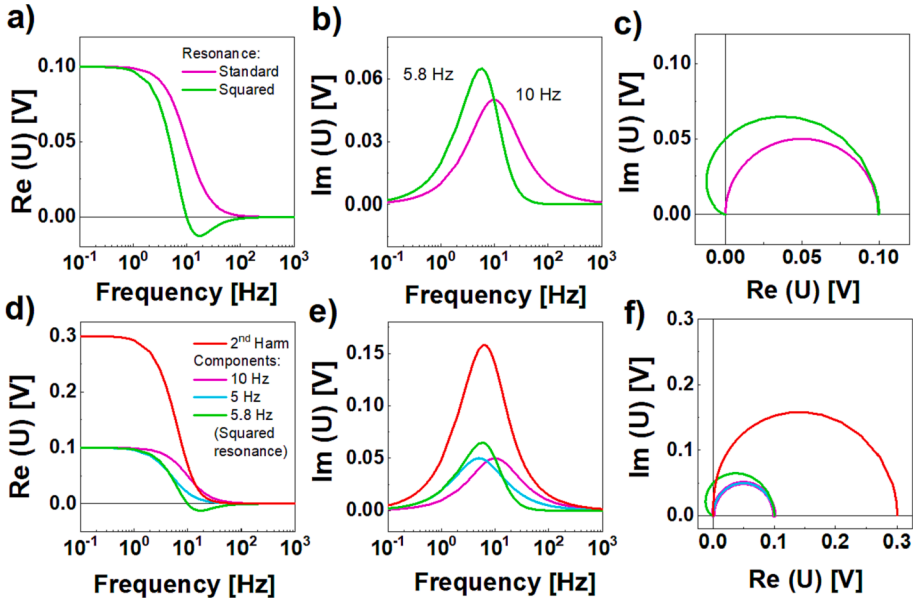

Fig. 3. Real (a), imaginary (b) and Nyquist (c) plots comparing the squared resonance to the standard resonance with constants; Real (d), imaginary (e) and Nyquist (f) spectra of the IMVS second harmonics simulated for the model of second order recombination. Deconvolution is performed according to **Equation (31)** with constants: k' = 10 Hz, A = B = 100 μA, E = 1000 μA/s, C = 100 μF.

and j(t) the current measured by the external circuit. Per analogy, the second equation quantifies the Q_H charge flow in the Hemlholtz layer with k_{CT} being charge transfer rate i.e., the rate of charge flow from the semiconductor into the electrolyte. The third equation is simply Kirchoff's law for the system.

With the assumption of Gartner equation, a single complex exponential is a solution for the current and charges Q_H and Q_{SC}. In this case, one can get the expression for AC component of the current, measured in the IMPS [39]:

$$j(\omega) = I^0 \frac{C_H(i\omega + k_R + k_{CT}) + C_{SC}(i\omega + k_{CT} - k_R)}{(i\omega + k_R + k_{CT})(i\omega C_H C_{SC} R + C_H + C_{SC})} \tag{33}$$

This result gives two characteristic time constants manifesting as two extrema on the imaginary part of the spectrum (or two semicircles on the Nyquist plot). In simplification, the high frequency one corresponds to the transport and low frequency to the recombination/charge transport characteristic times. It is possible to extend the two-resonance model for higher harmonics by introducing the intensity-dependent generation current. If the Taylor-like expressions are plugged into initial set of differential equations, a single complex exponential is no longer a valid solution. In the following case, the solution for the Q_H, Q_{SC} and current would be also series of exponentials:

$$\begin{cases} Q_{SC}(t) = \sum_{n=0}^{\infty} {Q_{SC}}^{(n)} \exp(i\omega n t) \\ Q_H(t) = \sum_{n=0}^{\infty} {Q_H}^{(n)} \exp(i\omega n t) \\ j(t) = \sum_{n=0}^{\infty} j^{(n)} \exp(i\omega n t) \end{cases} \tag{34}$$

After plugging those expressions into the set of kinetic equations (32) and rugging out the time dependence, one can obtain expressions for the n-th harmonics of the current $j^{(n)}$:

$$j^{(n)}(\omega) = I^{(n)} \frac{C_H(i\omega n + k_R + k_{CT}) + C_{SC}(i\omega n + k_{CT} - k_R)}{(i\omega n + k_R + k_{CT})(i\omega n C_H C_{SC} R + C_H + C_{SC})} \tag{35}$$

For n = 1, the expression of the first harmonic is fully reduced to the fundamental case in the **Equation (33).** According to this formula, each next harmonic should have a decaying amplitude, and the decay profile should match the Taylor expansion coefficients $I^{(n)}$ in **Equation (15)**. Moreover, in this solution the spectrum of every harmonic should have the same number of time constants equal to 2 and those characteristic frequencies should decay with the number of harmonics as a simple reciprocal relation:

$$\omega_{LF}(n) = \frac{k_R + k_{CT}}{n} \tag{36}$$

$$\omega_{HF}(n) = \frac{1}{nRC} = \frac{k_{tr}}{n} \tag{37}$$

where LF stands for low frequency extremum and HF for high frequency maximum, C is a series sum of capacitances C_H and C_{SC}. Graphical representation of the spectra is shown in Fig. 4. Depending on the relations between k_{CT} and k_R, LF can exhibit maximum or minimum. In this example, $k_{CT} < k_R$ therefore, the low-frequency arc has a negative imaginary part for every harmonic. Summarizing, if the intensity-dependent generation is assumed in the two resonance case, each of two characteristic frequencies behave exactly the same way as in the single resonance case. Analogous solution for the two-resonance case in IMVS consists of single arc, which is visualized in Fig. 4 **d–f.** Full solution is contained in ESI file in Section 9**.**

Besides intensity-dependent generation, one can install intensity-dependence of recombination rate (or charge transfer rate or the transport rate) or the higher order rates for the two-resonance case as well. However, inclusion of each additional component makes mathematics increasingly complicated. Experimental higher harmonic spectra do not always follow relations derived from those models, as they are composed of many superimposed resonances. Nevertheless, they provide a benchmark for qualitative analysis of more complicated cases. The following algorithm (Scheme 2) has been proposed to distinguish between the behavior related to each model based on experimental results. This procedure will be demonstrated in the next sections with a silicon photodiode and a photoelectrochemical cell with TiO_2 nanotubes as a working electrode.

Finally, it is likely that the presented HHA formalism can be integrated with other recently published developments of the IMPS/IMVS techniques. For instance, in IMPS microscopy giving insight into structural heterogeneities of the photoactive materials and solar cells [17], HHA would resolve the physical source of nonlinear effects. Combined modulated techniques such as light intensity modulated impedance spectroscopy (LIMIS) can be the second path to apply the HHA instead of (or in parallel to) the commonly used EC approach [59–61].

5. Results and discussion

5.1. Si photodiode

Higher harmonic IMVS spectra of the Si photodiode in the Bode and Nyquist projections are presented in Fig. 5. It is easy to see that the fundamental frequency exhibits one peak and one shoulder on the imaginary part, located at ca. 260 Hz and at ca. 30 Hz, respectively – these will be abbreviated as high-frequency and low-frequency peaks. In fact, the imaginary part of the first harmonic can be decomposed into two Lorentzians centered at 262 Hz and 32 Hz.. Most probably, they correspond to two possible mechanisms of recombination with the 250 Hz one dominating in the response. The general shape of the spectra shows good agreement with the simplest solution written in **Equation (23)** and Fig. 1 **d-f** evidencing the nonlinear generation current.

Subtle deviations from the simplest model can originate from either the intensity-dependent recombination or second-order recombination. One of the marks is overshooting of real parts to the negative values [12 32] after exceeding 100 Hz. Actually, it is not possible to fit only simple Lorentzians to the second (and higher) harmonic. The imaginary part seems to be well-fitted only when both simple and squared resonances are used – then, asymmetric shape of the HF peak is resolved (see Section 10 in ESI file Figure S2-3). Deconvoluted peaks of squared resonances are located at 32 Hz and 260 Hz, almost exactly as fundamentals. Therefore, both recombination pathways (LF and HF) are most likely second-order due to the higher harmonics are not composed purely of Lorentzians.

The photovoltage – intensity profile in Fig. 6**a** is clearly nonlinear, which justifies the presence of higher harmonics. As a result, with a high AC component of the power density (750 μW) up to 10th harmonics have a non-zero measurable frequency dispersion. A total amplitude at the low-frequency limit ($\omega \sim 0$) of the IMVS response exhibits a monotonous power-law decay with a power coefficient equal to −0.5 (Fig. 6**b)**. Such behavior agrees with the assumption of Taylor series convergence introduced earlier. It is to be noted that strong nonlinearities and higher harmonics appear even for (monochromatic) illuminations as small as 1 mW/cm^2, which are two orders of magnitude smaller than the typical solar simulators.

Besides the amplitude plot, identification of the harmonic content can be also performed qualitatively based on the time dependencies for the photovoltage U(t) or photocurrent I(t). Exemplar photovoltage time response for the Si photodiode data is given in ESI file (**Section** 11, Figure S4-5). It is easy to see that the stimulus (yellow) is a single sine, however, the response shape deviated drastically from sine. Considering that the deviation from the sine shape is severe, it is expected that the second and higher harmonic would be present along with the fundamental. This is confirmed on the amplitude plot in Fig. 6**b.**

Furthermore, a series of experiments with different AC illumination intensities was carried out on the same Si photodiode (Fig. 7). The power

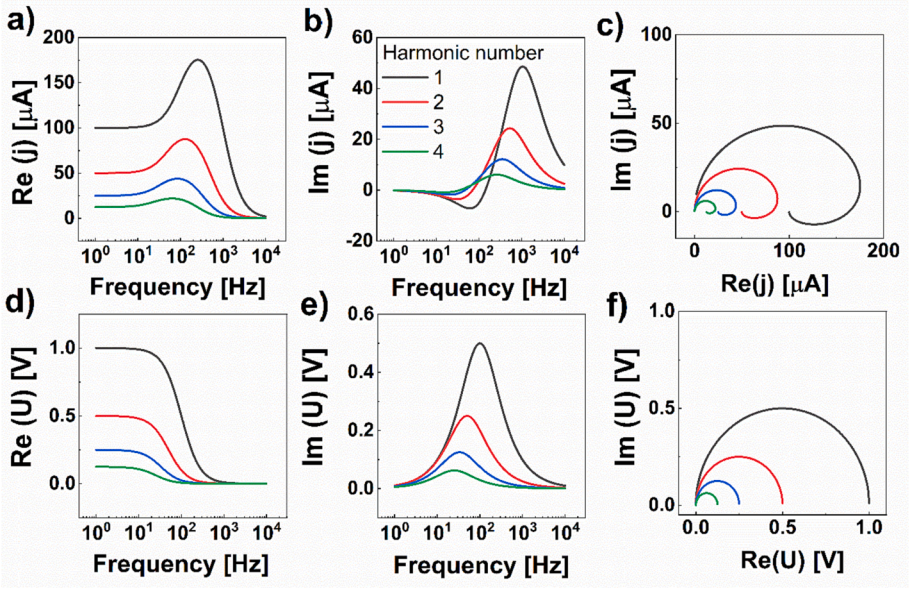

Fig. 4. Higher harmonics spectra of IMPS and IMVS simulated for the model of two resonances with intensity-dependent generation. Constants used for construction of plots: k_R = 100 Hz, k_{CT} = 0.1 Hz, $C_H = 10^{-5}$F, $C_{sc} = 10^{-6}$F, R = 10 [3] Ω, $I^{(1)}$ = 100 μA, $I^{(2)}$ = 50 μA, $I^{(3)}$ = 25 μA, $I^{(4)}$ = 12.5 μA.

density is expressed as the percentage of the maximum intensity of the LED in the device, which is equal to ca. 1800 μW. Apparently, the sample possesses the HF constant at both small and large illuminations, however the low-frequency recombination mechanism manifests only at the highest power. This observation strongly suggests the necessity of using high values of AC components to fully understand the sample behavior, in contrast to the commonly used linear approximation that requires a small perturbation. The second and third harmonic requires the AC component of light intensity to be at least 20 % of the maximum to be distinguished from the noise and the fourth harmonic – 30 %. This threshold for higher harmonic appearance increases with the harmonic number but even at the 2 % of the AC, the second harmonic is strongly present indicating an intrinsic nonlinearity of the system (see **ESI Figure S6, Section 12**). In other words, the AC stimulus is presumably never small enough to produce only the first harmonic for real systems.

According to the fit in Fig. 7**c,** IMVS harmonic amplitudes at the low-frequency limit increases exponentially with the AC component of the stimulus. The general shape of this profile for each harmonic is difficult to assess from the proposed theory – it can be basically any analytic function depending on the values of Taylor coefficients. This issue is discussed in the **ESI file in Section 13.** Interestingly, the exponent obtained by fitting of the experimental data is the same for all harmonics other than the fundamental. It might suggest that among the harmonics, the first one is the most 'contaminated' with parasitic processes that distort the relationship.

TiO_2 nanotubes.

TiO_2 nanotubes (TNTs) were chosen as an exemplary metal oxide nanostructured semiconductor to be a second toy model for HHA – in this case applied to IMPS measurements. Higher harmonic spectra of the IMPS response for TNTs samples were measured at + 1000 mV polarization unless stated otherwise and are presented in Fig. 8. Technically, such measurements should be performed under short-circuit conditions to avoid non-photocurrent contributions. Argumentation on the choice of such potential is given in **Section 14 of the ESI file**. Briefly, although it is not a short circuit potential, it is sufficiently high to generate a photocurrent that is not limited by the potential [50]. In all cases, the current has been recalculated to the current density by dividing the constant sample area equal to 3.14 cm^2.

The fundamental response exhibits four characteristic time constants located at 724 Hz, 94.7 Hz, 21 Hz and 15 mHz all exhibiting positive imaginary parts. The analysis will be focused only on the two HF features related to transport. Xiao et al. reported the transport characteristic frequency at 300 Hz for titania nanoparticles and 200 Hz for titania nanowires using 11 mW cm^{-2} intensity [50]. In other works, the extremum frequency for dye sensitized solar cells based on TiO_2 oscillates between 100 and 200 Hz depending on the light intensity used [34] and between 70 and 350 Hz depending on the layer and preparation method [35]. The suggested initial interpretation of those signals would be the recombination/charge transfer arcs at low frequency and two distinct transport pathways at high frequency. Alternatively, those two high-frequency constants can originate from different mobilities of electrons and holes [62]. The presence of surface states not involved in electron transfer (deep traps) producing an additional semicircle at the first quadrant [33] can be discarded in the case studied. This is because the polarization is strongly anodic and far from the potential region of photocurrent switching [17]. Regardless, it is to be noted that the high frequency limit exhibits the negative real parts strongly suggesting the presence of nonlinear phenomena. Moreover, the explanation involving negative slope of the photocurrent-power density profile can be ruled out, because it is certainly positive in the studied range of power densities (see Fig. 9**c**).

The second harmonic exhibits markedly different behavior than the fundamental, as the two transport maxima change into a complex series of peaks with several apparent extrema. Fitting of pure Lorentzians was performed to resolve the positions of minima and maxima. The result of the fitting are overlapped 5 Hz maximum, 85 Hz minimum, and 115 Hz maximum. No higher-order resonances were necessary to obtain fitting, although its quality is relatively low due to low-frequency features being difficult to model. It is strongly suggested that second-order recombination can be ruled out. Moreover, the real part exhibits one minimum and one maximum instead of a monotonous decay with inflections. In the Nyquist projection, it gives a unique sigma-like shape with at least five extrema occupying all four quadrants of the complex plane. It is to be noted that the emergence of additional extrema for higher harmonics is indicative of the intensity dependence recombination model. It corresponds to the case, when both A and B constants in the expression for $Q^{(2)}$ are negative (Fig. 2 – brown curve). Slightly different behavior can be observed for the third and fourth harmonics as the low-frequency regions of the real parts are negative. Imaginary part is well modelled by the series of first-order resonances suggesting that higher order

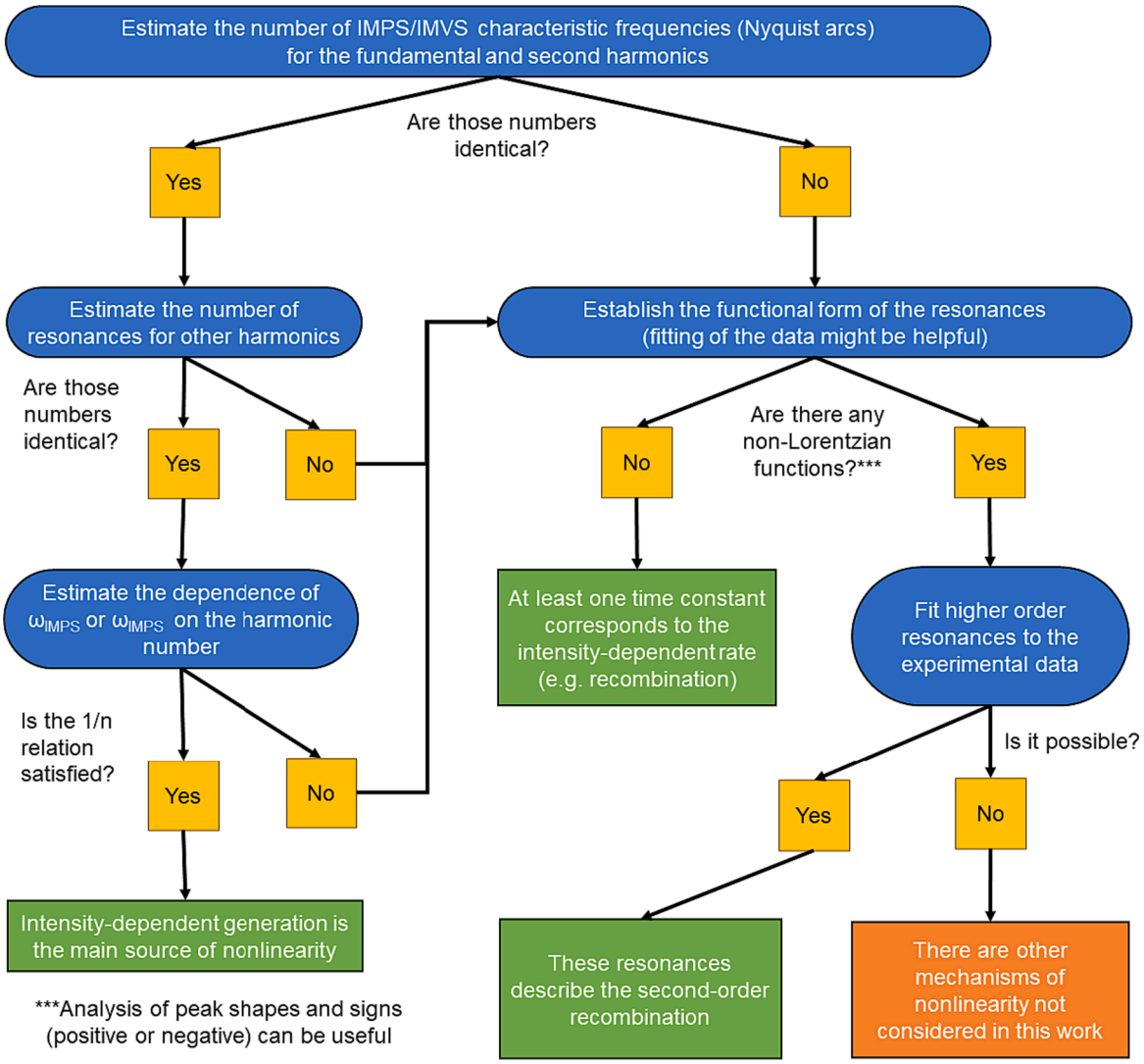

Scheme 2. Algorithm for qualitative analysis of IMPS/IMVS higher harmonic spectra towards estimating the source of nonlinearity.

recombination is not present. Simultaneously occurring negative real and negative imaginary part are equivalent to the Nyquist plot occupying mostly the third quadrant. It is difficult to discern contributions coming from the generation, recombination or transport using solely qualitative analysis. However, considering the frequency range between 10 Hz and 1000 Hz, the most dominant contribution is presumably transport. Nevertheless, if there was only the intensity-dependent generation, the number of frequencies on each harmonic would be the same. Thus, according to the models given in the Theory section, the presence of both intensity-dependent generation and transport is evidenced.

A more detailed analysis of higher harmonics shapes is contained in Fig. 9. As recorded amplitudes of higher harmonics are markedly lower than the fundamental, in the following figure the first harmonic is omitted for the clarity of presentation. This observation is connected to the fact that the studied system is weakly non-linear (Fig. 9**c**) in contrast to the photodiode and regardless of the applied potential.

On the exemplar photocurrent time profile in Figure S4-5 the deviation of the response from the sine shape is rather mild compared to the photodiode. Nevertheless, the photocurrent response is not an ideal sine and higher harmonics are indeed present. Magnitudes of them are two orders of magnitude smaller than the fundamental, though.

It is to be noted that although the second and third harmonic possess a higher number of characteristic constants connected to the transport, this number is reduced to two again for harmonics 4 and higher. Moreover, as both real and imaginary parts are negative for those functions, all of them should contribute to the fundamental leading to the observed "negative resistance". The amplitudes of harmonics higher than 2 decrease almost linearly with the harmonic number, in contrast to the power-law decay observed for the IMVS measurement of the photodiode (Fig. 6**d**). The characteristic apparent LF constants and HF constants both decrease according to the power law, but with slightly different exponents equal to −2.7 and −2.4, respectively. Interestingly, the decay is faster than in the case of the simplest model given in equation (15) and Fig. 1. indicating intensity-dependent rate.

In Fig. 10, a series of HHA measurements is performed for different values of the AC component of the light stimulus. It is easy to see that the shapes of both the real and imaginary parts for the first harmonic do not change significantly with the varying AC component - only the amplitude increases almost linearly (Fig. 10 **b**).

On the other hand, in higher harmonics the HF extremum at the 100–500 Hz regime plummets for smaller AC, but the LF extremum at 10–60 Hz changes its sign and decreases its characteristic frequency with the AC component. In general, the decrease of the LF characteristic time constant indicates that one of the transport pathways in TiO_2 sample is slightly slower (increased transport resistance) for higher illumination intensities. This trend is repeated for all harmonics and more pronounced than for the fundamental. This outcome is contrary to the standard intuition and experimental data obtained solely from the

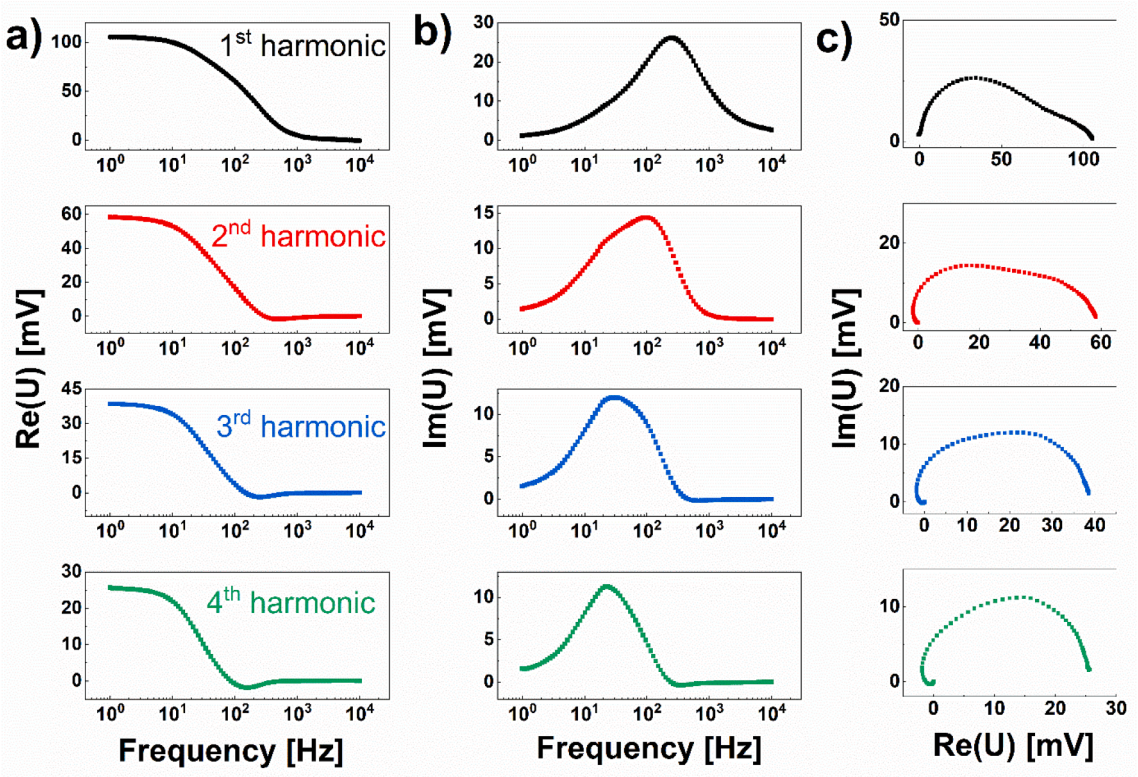

Fig. 5. Higher harmonic IMVS spectra of the Si photodiode in Bode and Nyquist projections recorded with DC and AC power density equal to 750 μW.

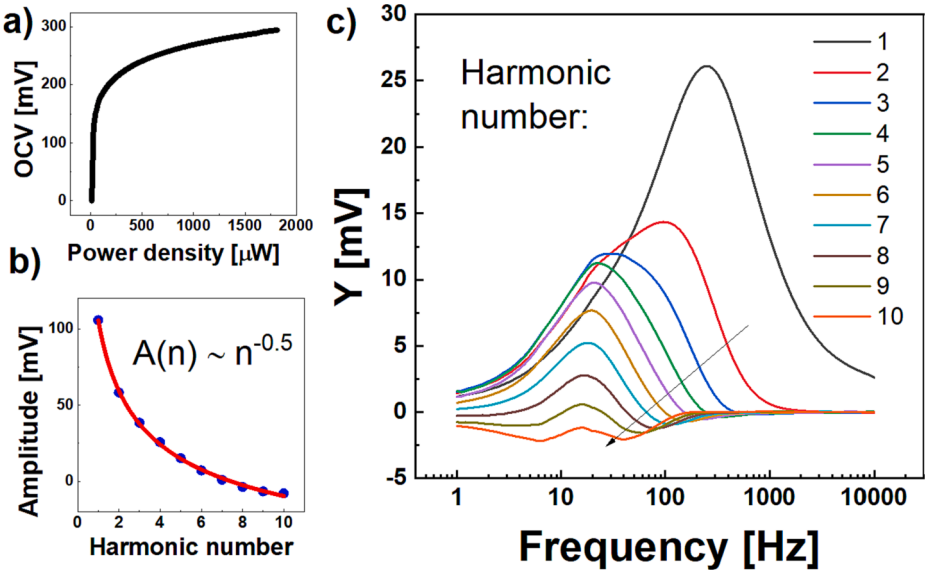

Fig. 6. A) Photovoltage dependence on the illumination intensity, b) decay profile of the IMVS amplitude at the low-frequency limit, c)) imaginary part of higher harmonics of IMVS spectra from 1 to 10, arrows indicate the increasing number of harmonics.

fundamental harmonic [43,50–52]. A general physical intuition is that the resistance should decrease with higher number of mobile charges generated during photoexcitation. However, there are works with results similar to ours [42]. This property of increased resistance might be intrinsic to the studied sample. However, it is also possible that many other photoactive materials could behave similarly in the higher harmonics approach, because results obtained from solely the first harmonic can be misleading in correct description of intensity-dependence.

Lastly, the influence of the electrode potential on the shape of the higher harmonics was established and gathered in Fig. 11. In general, in the models developed in the theoretical section there was no need to assume any explicit dependence of physical quantities on the potential to obtain the shape of the higher harmonics. The problem is easy in the case of the two-electrode measurements, where in the short-circuit conditions, the voltage is exactly zero. However, to solve many problems in photoelectrochemistry, there is a strong need to operate in a three-electrode system with a potentiostat. Therefore, it is desirable to understand higher harmonic response also in this set-up. It is known that the charge transfer rate and the recombination rate should depend on the electrode potential somehow. In the case of metal | electrolyte

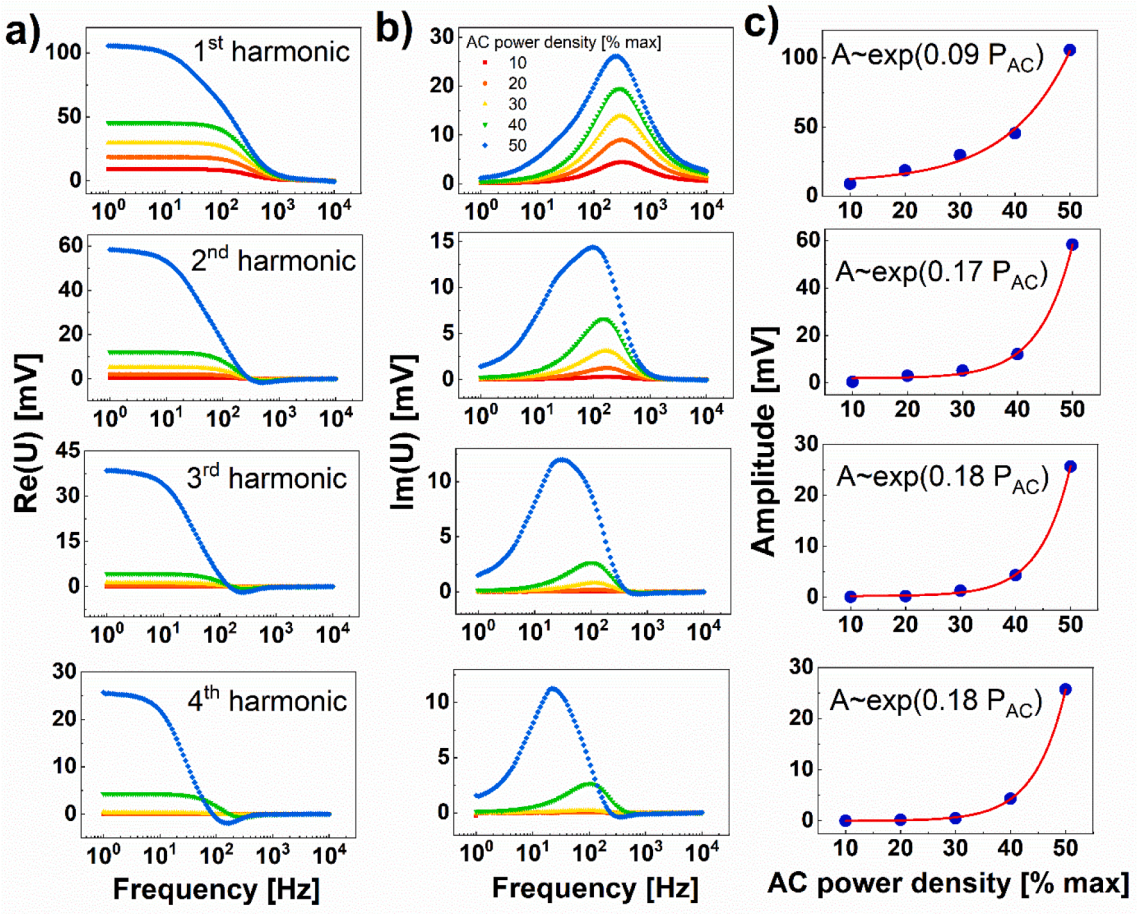

Fig. 7. A-b) higher harmonic imvs spectra of the si photodiode with varying ac component of the light; c) corresponding profiles of the amplitude decay at the low frequency limit. spectra were recorded with dc component of the light power density equal to 50 % (750 μW) and AC component to 50 %, 40 %, 30 %, 20 % and 10 % of the maximum intensity.

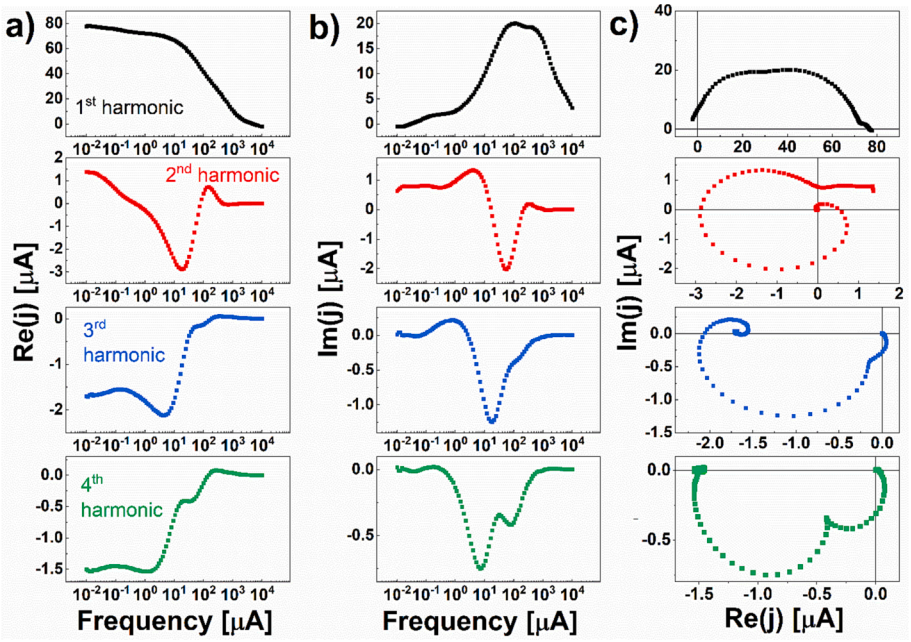

Fig. 8. Higher harmonic IMPS spectra of TNTs in Bode and Nyquist projections recorded with DC and AC power density equal to 750 μW and + 1000 mV electrode potential.

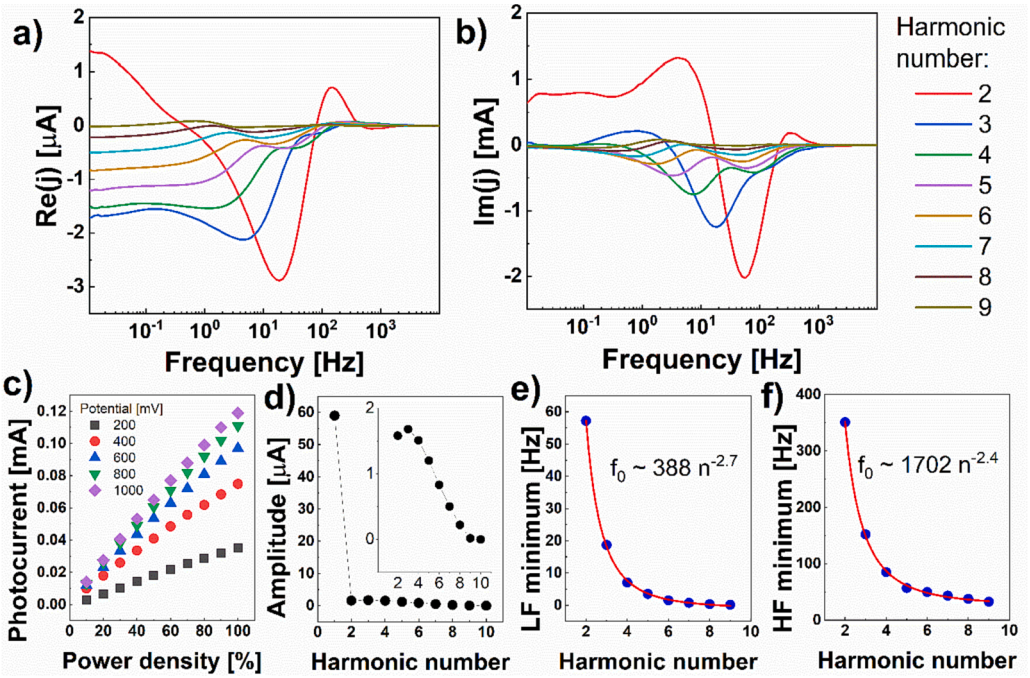

Fig. 9. a)-b) HHA of the real and imaginary part of the IMPS response of TiO_2. c) Intensity-photocurrent profiles for different electrode potentials showing weak-nonlinear regime, d) decay profile of the LF limit of the amplitude, e)-f) decay profile of the transport characteristic frequencies.

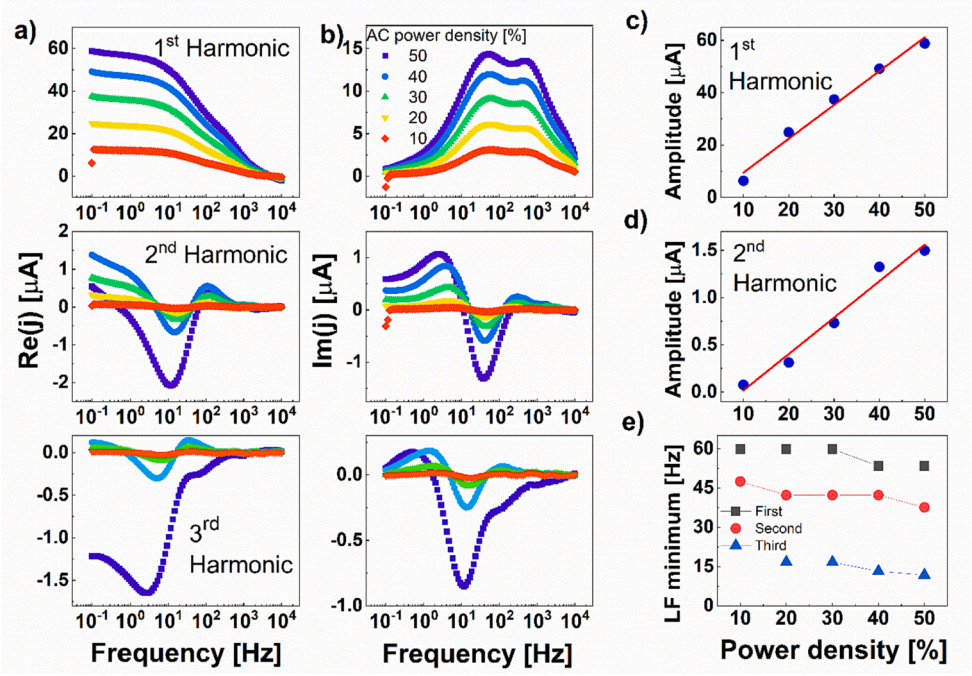

Fig. 10. A)-b) higher harmonic imps spectra of tnts with different ac component c)-d) corresponding profiles of the amplitude decay at the low frequency limit, e) variation of the low-frequency time constant with respect to the ac component. spectra were recorded with dc component of the light power density equal to 50 % (750 μW) and AC component to 50 %, 40 %, 30 %, 20 % and 10 % of the maximum intensity.

interfaces, the charge transfer rate is typically assumed to be exponential based on the Butler-Volmer equation, or Gaussian in the Marcus theory. In the case of semiconductors however, those models cannot be translated directly, as the voltage drop occurs both in the Helmholtz layer and in the space charge region. A reliable theoretical description of the potential dependence for quantities such as the charge transfer rate, recombination rate and transport rate are still missing.

Nevertheless, there are plenty of experimental approaches that have touched on this issue involving IMPS/IMVS, transient photocurrent/photovoltage, and photoimpedance electrochemical spectroscopy (PEIS). Some PEIS studies of hematite electrodes suggest parabolic (or polynomial) shape of the charge transfer and recombination rates [54], others report monotonous growth of the rate constant and parabolic shape of the recombination [53]. In case of TiO_2, the charge transfer is

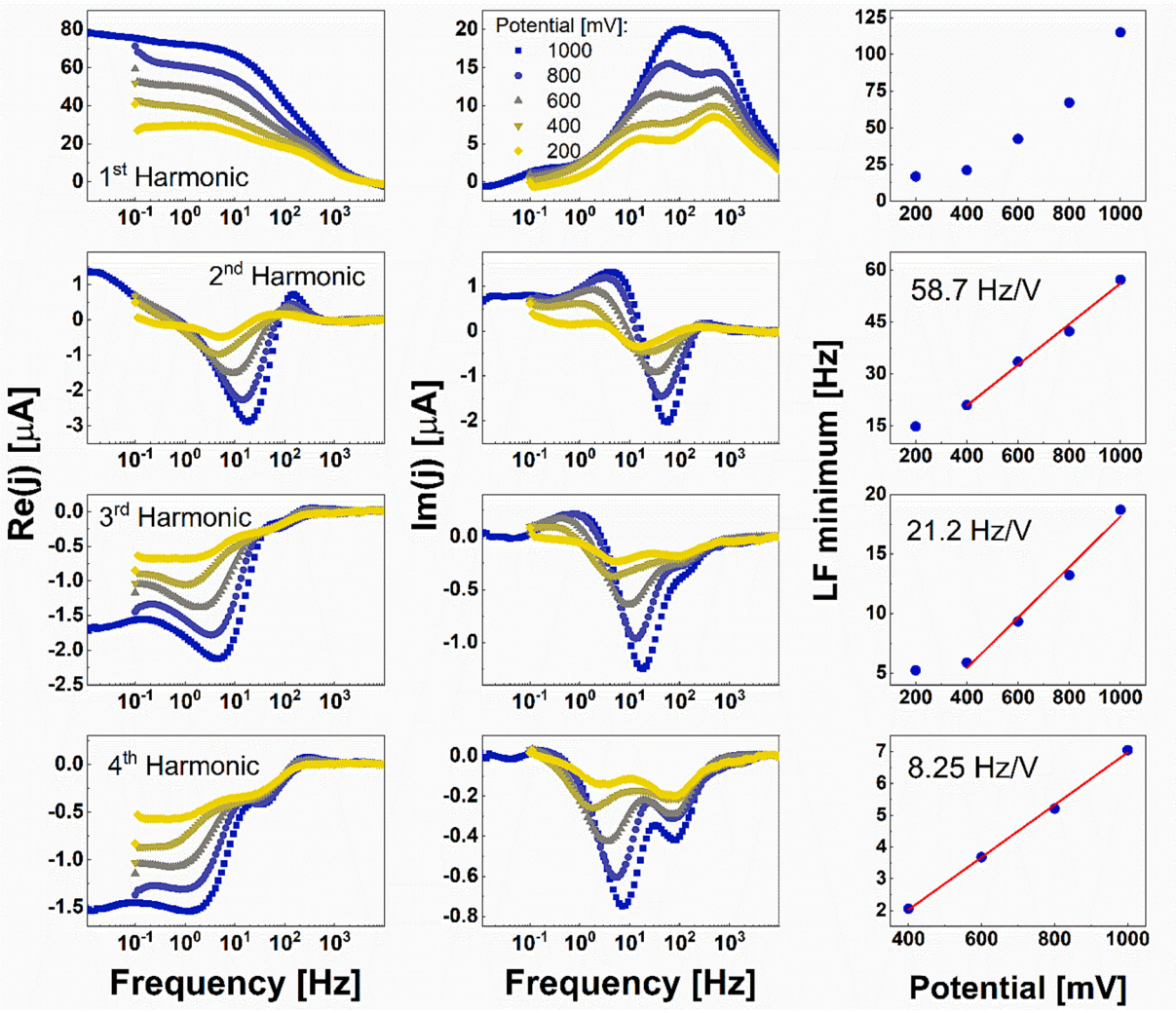

Fig. 11. Higher harmonic IMPS spectra of TNTs and corresponding profiles of the low-frequency decay with potential. Spectra were recorded with DC and AC component of the light power density equal both 50 % (750 μW) and electrode potentials were set to 200, 400, 600, 800 and 1000 mV.

constant or increasing depending on the pH, while recombination generally plummets with larger anodic polarization [63]. In the case of perovskite MAPI (methylammonium-lead-iodide) photoelectrochemical cells, both rates (including transport) seem to increase with the electrode potential [13]. In general, one can safely assume that the recombination rate decreases with electrode potential because of the larger electric field inside the space-charge region facilitating separation. Then, the charge transfer rate and transport rate are expected to have opposite trend for the same reason [41] as the potentiostat provides an additional driving force for the (photo)current flow.

Nevertheless, HHA allows a phenomenological analysis of the potential dependence of the rates in the following way. As discussed before, the first harmonic of the IMPS response exhibits two characteristic frequencies (Fig. 11**b** – imaginary part) and both increase nonlinearly with the applied potential accompanied with higher amplitudes. In other words, transport is faster, and the photocurrents are greater when the potential of titania is more anodic. This is in accordance with the physical intuition that the higher electric field in the space charge region facilitates separation of excitons, which results in a higher photocurrent and lower transport resistance. This pattern is analogous for all harmonics - all extrema lie at higher frequency as the potential is more anodic. The slope of those lines also decreases with the harmonic number. In other words, there is an individual potential dependence for each coefficient in the Taylor expansion of the intensity-dependent recombination/transport. Interestingly, electrode potential does not change numbers and signs of extrema in the studied sample confirming that the developed mathematical formalism is indifferent to the electrode potential.

6. Conclusions

In this work, an approach for the analysis of nonlinearities in photoelectrochemical and photovoltaic systems using higher harmonic analysis was proposed. A series of analytical solutions of kinetic equations were developed for higher harmonics that originate from either intensity-dependent generation current, recombination rate, transport rate or second order recombination. Those solutions constitute a mathematical model for interpretation of semiconductor photophysics based on experimentally obtained harmonics of IMPS and IMVS spectra.

This approach was applied for analysis of two exemplar cases – IMVS of the Si photodiode and IMPS for the photoelectrochemical cell with the TiO_2 nanotubes as the working electrode. The method allowed to recognize the two different recombination rates for the photodiode both second order. In the case of TiO_2, it allowed to distinguish two characteristic transport frequencies and their intensity-dependence. Decrease of those rates with the power density of illumination is more evident for higher harmonics than for the fundamental and contrasting with other studies.

A series of arguments for the limited applicability of the first harmonic for studying intensity-dependent quantities was presented. Although their mathematics is more complicated, the higher harmonic analysis possesses a greater explanatory power for investigating recombination and transport mechanisms that can be used for studies of complex photoelectrochemical and photovoltaic systems. Similarly to the recently introduced IMPS microscopy giving insight into structural heterogeneities, HHA is anticipated to solve physical features underlying behavior of the photoactive materials and solar cells. There is also a possibility to integrate the HHA formalism with the combined modulated techniques such as light intensity modulated impedance spectroscopy.

CRediT authorship contribution statement

Adrian Olejnik: . **Katarzyna Grochowska:** Funding acquisition, Resources, Supervision, Writing – original draft, Writing – review & editing.

Declaration of Competing Interest

The authors declare the following financial interests/personal relationships which may be considered as potential competing interests: [Adrian Olejnik reports financial support was provided by Ministry of Education and Science of the Republic of Poland. Katarzyna Grochowska reports financial support was provided by National Science Centre Poland. Adrian Olejnik reports a relationship with Instytut Fotonowy that includes: non-financial support].

Data availability

The dataset underlying this work is openly available in Zenodo repository under the following persistent link: https://doi.org/10.5281/zenodo.10209375.

Acknowledgements

This work was financially supported by the Polish Ministry of Science and Higher Education through Diamentowy Grant DI 2019 017649 and by the National Science Center through OPUS grant no 2021/41/B/ST8/01849. The authors greatly appreciate the technical assistance provided from Instytut Fotonowy.

Appendix A. Supplementary data

Supplementary data to this article can be found online at https://doi.org/10.1016/j.measurement.2023.113943.

References

[1] L. Wang, M. Schmid, J.B. Sambur, Single nanoparticle photoelectrochemistry: What is next? J. Chem. Phys. 151 (18) (2019) 180901, https://doi.org/10.1063/1.5124710.
[2] Z. Najaf, D.L.T. Nguyen, S.Y. Chae, O.-S. Joo, A.U.H.A. Shah, D.-V.-N. Vo, V.-H. Nguyen, Q.V. Le, G. Rahman, Recent trends in development of hematite (α-Fe2O3) as an efficient photoanode for enhancement of photoelectrochemical hydrogen production by solar water splitting, Int. J. Hydrogen Energy 46 (45) (2021) 23334–23357, https://doi.org/10.1016/j.ijhydene.2020.07.111.
[3] M.Q. Khokhar, H. Yousuf, S. Jeong, S. Kim, X. Fan, Y. Kim, S.K. Dhungel, J. Yi, A Review on P-type tunnel oxide passivated contact (TOPCon) solar cell, Trans. Electr. Electron. Mater. (2023), https://doi.org/10.1007/s42341-023-00433-z.
[4] M.Q. Khokhar, S.Q. Hussain, M.A. Zahid, D.P. Pham, E.-C. Cho, J. Yi, Numerical simulation and experiment of a high-efficiency tunnel oxide passivated contact (TOPCon) solar cell using a crystalline nanostructured silicon-based layer, Appl. Sci. 12 (1) (2021) 392, https://doi.org/10.3390/app12010392.
[5] M.Q. Khokhar, K. Mallem, X. Fan, Y. Kim, S.Q. Hussain, E.-C. Cho, J. Yi, Experimental and numerical simulation of molybdenum oxide films with wide bandgap and high work function for carrier-selective contact solar cells, ECS J. Solid State Sci. Technol. 11 (8) (2022) 085001, https://doi.org/10.1149/2162-8777/ac8372.
[6] M.Q. Khokhar, S.Q. Hussain, S. Kim, S. Lee, D.P. Pham, Y. Kim, E.-C. Cho, J. Yi, Review of rear emitter silicon heterojunction solar cells, Trans. Electr. Electron. Mater. 21 (2) (2020) 138–143, https://doi.org/10.1007/s42341-020-00172-5.
[7] S. Vibavakumar, K.D. Nisha, S. Harish, J. Archana, M. Navaneethan, Synergistic effect of MoO3/MoS2 in improving the electrocatalytic performance of counter electrode for enhanced efficiency in dye-sensitized solar cells, Mater. Sci. Semicond. Process. 161 (2023) 107431, https://doi.org/10.1016/j.mssp.2023.107431.
[8] M. Pylnev, F. Rezende Santos, D. Zhang, H. Alawadhi, N. Tabet, Compact TiO2 Layer by UV-assisted TiBr 4 chemical bath deposition for perovskite solar cells, Mater. Sci. Semicond. Process. 161 (2023) 107467, https://doi.org/10.1016/j.mssp.2023.107467.
[9] F. Finger, K. Welter, F. Urbain, V. Smirnov, B. Kaiser, W. Jaegermann, Photoelectrochemical water splitting using adapted silicon based multi-junction solar cell structures: development of solar cells and catalysts, upscaling of combined photovoltaic-electrochemical devices and performance stability, Z. Phys. Chem. 234 (6) (2020) 1055–1095, https://doi.org/10.1515/zpch-2019-1453.
[10] S. Pishgar, S. Gulati, J.M. Strain, Y. Liang, M.C. Mulvehill, J.M. Spurgeon, In Situ analytical techniques for the investigation of material stability and interface dynamics in electrocatalytic and photoelectrochemical applications, Small Methods 5 (7) (2021) 2100322, https://doi.org/10.1002/smtd.202100322.
[11] J. Cen, Q. Wu, M. Liu, A. Orlov, Developing new understanding of photoelectrochemical water splitting via in-situ techniques: A review on recent progress, Green Energy Environ. 2 (2) (2017) 100–111, https://doi.org/10.1016/j.gee.2017.03.001.
[12] D. Cardenas-Morcoso, A. Bou, S. Ravishankar, M. García-Tecedor, S. Gimenez, J. Bisquert, Intensity-modulated photocurrent spectroscopy for solar energy conversion devices: What does a negative value mean? ACS Energy Lett. 5 (1) (2020) 187–191, https://doi.org/10.1021/acsenergylett.9b02555.
[13] S. Ravishankar, A. Riquelme, S.K. Sarkar, M. Garcia-Batlle, G. Garcia-Belmonte, J. Bisquert, Intensity-modulated photocurrent spectroscopy and its application to perovskite solar cells, J. Phys. Chem. C 123 (41) (2019) 24995–25014, https://doi.org/10.1021/acs.jpcc.9b07434.
[14] N. Parikh, S. Narayanan, H. Kumari, D. Prochowicz, A. Kalam, S. Satapathi, S. Akin, M.M. Tavakoli, P. Yadav, Recent progress of light intensity-modulated small perturbation techniques in perovskite solar cells, Physica Rapid Research Ltrs 16 (4) (2022) 2100510, https://doi.org/10.1002/pssr.202100510.
[15] D. Ruelle, A review of linear response theory for general differentiable dynamical systems, Nonlinearity 22 (4) (2009) 855–870, https://doi.org/10.1088/0951-7715/22/4/009.
[16] A. Goossens, D.D. Macdonald, A photoelectrochemical impedance spectroscopic study of passive metals, Electrochim. Acta 38 (14) (1993) 1965–1968, https://doi.org/10.1016/0013-4686(93)80324-S.
[17] J.S. Laird, S. Ravishankar, K.J. Rietwyk, W. Mao, U. Bach, T.A. Smith, Intensity modulated photocurrent microspectrosopy for next generation photovoltaics, Small Methods 6 (9) (2022) 2200493, https://doi.org/10.1002/smtd.202200493.
[18] A. Bou, H. A¯boliņš, A. Ashoka, H. Cruanyes, A. Guerrero, F. Deschler, J. Bisquert, Extracting *in situ* charge carrier diffusion parameters in perovskite solar cells with light modulated techniques, ACS Energy Lett. 6 (6) (2021) 2248–2255, https://doi.org/10.1021/acsenergylett.1c00871.
[19] A. Bou, A. Pockett, H. Cruanyes, D. Raptis, T. Watson, M.J. Carnie, J. Bisquert, Limited information of impedance spectroscopy about electronic diffusion transport: The case of perovskite solar cells, APL Mater. 10 (5) (2022) 051104, https://doi.org/10.1063/5.0087705.
[20] J. Bisquert, M. Janssen, From frequency domain to time transient methods for halide perovskite solar cells: The connections of IMPS, IMVS, TPC, and TPV, J. Phys. Chem. Lett. 12 (33) (2021) 7964–7971, https://doi.org/10.1021/acs.jpclett.1c02065.
[21] D. Bernhardsgrütter, M.M. Schmid, Modeling of intensity-modulated photocurrent/photovoltage spectroscopy: Effect of mobile ions on the dynamic response of perovskite solar cells, J. Phys. Chem. C 123 (50) (2019) 30077–30087, https://doi.org/10.1021/acs.jpcc.9b08457.
[22] E.L. Spera, C.J. Pereyra, Y. Di Iorio, M. Berruet, M. Vazquez, R.E. Marotti, Charge dynamics in CuInS2 photovoltaic devices with In2S3 as buffer layer, Mater. Chem. Phys. 282 (2022) 125871, https://doi.org/10.1016/j.matchemphys.2022.125871.
[23] M. Kiel, O. Bohlen, D.U. Sauer, Harmonic analysis for identification of nonlinearities in impedance spectroscopy, Electrochim. Acta 53 (25) (2008) 7367–7374, https://doi.org/10.1016/j.electacta.2008.01.089.
[24] N. Xu, J. Riley, Nonlinear analysis of a classical system: The double-layer capacitor, Electrochem. Commun. 13 (10) (2011) 1077–1081, https://doi.org/10.1016/j.elecom.2011.07.003.
[25] F. Fasmin, R. Srinivasan, Review—Nonlinear electrochemical impedance spectroscopy, J. Electrochem. Soc. 164 (7) (2017) H443–H455, https://doi.org/10.1149/2.0391707jes.
[26] N. Xu, D.J. Riley, Nonlinear analysis of a classical system: The faradaic process, Electrochim. Acta 94 (2013) 206–213, https://doi.org/10.1016/j.electacta.2013.01.141.
[27] J. Wawrzyniak, K. Grochowska, J. Karczewski, P. Kupracz, J. Ryl, A. Dołęga, K. Siuzdak, The geometry of free-standing titania nanotubes as a critical factor controlling their optical and photoelectrochemical performance, Surf. Coat. Technol. 389 (2020) 125628, https://doi.org/10.1016/j.surfcoat.2020.125628.
[28] J. Wawrzyniak, J. Karczewski, E. Coy, I. Iatsunskyi, J. Ryl, M. Gazda, K. Grochowska, K. Siuzdak, Spectacular oxygen evolution reaction enhancement through laser processing of the nickel-decorated titania nanotubes, Adv. Mater. Interfaces 8 (1) (2021) 2001420, https://doi.org/10.1002/admi.202001420.

[29] J. Wawrzyniak, J. Karczewski, P. Kupracz, K. Grochowska, E. Coy, A. Mazikowski, J. Ryl, K. Siuzdak, Formation of the hollow nanopillar arrays through the laser-induced transformation of TiO2 nanotubes, Sci Rep 10 (1) (2020) 20235, https://doi.org/10.1038/s41598-020-77309-2.
[30] J. Wawrzyniak, J. Karczewski, P. Kupracz, K. Grochowska, K. Załęski, O. Pshyk, E. Coy, M. Bartmański, M. Szkodo, K. Siuzdak, Laser-assisted modification of titanium dioxide nanotubes in a tilted mode as surface modification and patterning strategy, Appl. Surf. Sci. 508 (2020) 145143, https://doi.org/10.1016/j.apsusc.2019.145143.
[31] K. Dashtian, S. Shahbazi, M. Tayebi, Z. Masoumi, A review on metal-organic frameworks photoelectrochemistry: A headlight for future applications, Coord. Chem. Rev. 445 (2021) 214097, https://doi.org/10.1016/j.ccr.2021.214097.
[32] A. Pockett, M. Spence, S.K. Thomas, D. Raptis, T. Watson, M.J. Carnie, Beyond the first quadrant: Origin of the high frequency intensity-modulated photocurrent/photovoltage spectroscopy response of perovskite solar cells, Sol. RRL (2021) 2100159, https://doi.org/10.1002/solr.202100159.
[33] M. Antuch, On the evolution of the intensity modulated photocurrent spectroscopy (IMPS) transfer function in quadrants (IV)-(I) or quadrants (II)-(III), Current Opinion Electrochemistry (2022) 101043, https://doi.org/10.1016/j.coelec.2022.101043.
[34] L. Dloczik, O. Ileperuma, I. Lauermann, L.M. Peter, E.A. Ponomarev, G. Redmond, N.J. Shaw, I. Uhlendorf, Dynamic response of dye-sensitized nanocrystalline solar cells: Characterization by intensity-modulated photocurrent spectroscopy, J. Phys. Chem. B 101 (49) (1997) 10281–10289, https://doi.org/10.1021/jp972466i.
[35] J. Halme, K. Miettunen, P. Lund, Effect of nonuniform generation and inefficient collection of electrons on the dynamic photocurrent and photovoltage response of nanostructured photoelectrodes, J. Phys. Chem. C 112 (51) (2008) 20491–20504, https://doi.org/10.1021/jp806512k.
[36] L.M. Peter, Dynamic aspects of semiconductor photoelectrochemistry, Chem. Rev. 90 (5) (1990) 753–769, https://doi.org/10.1021/cr00103a005.
[37] F.E. Bedoya-Lora, A. Hankin, G.H. Kelsall, *En Route* to a unified model for photo-electrochemical reactor optimisation. I - Photocurrent and H_2 yield predictions, J. Mater. Chem. A 5 (43) (2017) 22683–22696, https://doi.org/10.1039/C7TA05125E.
[38] T. Butburee, Y. Bai, H. Wang, H. Chen, Z. Wang, G. Liu, J. Zou, P. Khemthong, G.Q. M. Lu, L. Wang, 2D porous TiO 2 single-crystalline nanostructure demonstrating high photo-electrochemical water splitting performance, Adv. Mater. 30 (21) (2018) 1705666, https://doi.org/10.1002/adma.201705666.
[39] E.A. Ponomarev, L.M. Peter, A generalized theory of intensity modulated photocurrent spectroscopy (IMPS), J. Electroanal. Chem. 396 (1–2) (1995) 219–226, https://doi.org/10.1016/0022-0728(95)04115-5.
[40] E.A. Ponomarev, L.M. Peter, A comparison of intensity modulated photocurrent spectroscopy and photoelectrochemical impedance spectroscopy in a study of photoelectrochemical hydrogen evolution at P-InP, J. Electroanal. Chem. 397 (1–2) (1995) 45–52, https://doi.org/10.1016/0022-0728(95)04148-9.
[41] L.M. Peter, E.A. Ponomarev, D.J. Fermín, Intensity-modulated photocurrent spectroscopy: Reconciliation of phenomenological analysis with multistep electron transfer mechanisms, J. Electroanal. Chem. 427 (1–2) (1997) 79–96, https://doi.org/10.1016/S0022-0728(96)05033-4.
[42] A. Pockett, G.E. Eperon, T. Peltola, H.J. Snaith, A. Walker, L.M. Peter, P. J. Cameron, Characterization of planar lead halide perovskite solar cells by impedance spectroscopy, open-circuit photovoltage decay, and intensity-modulated photovoltage/photocurrent spectroscopy, J. Phys. Chem. C 119 (7) (2015) 3456–3465, https://doi.org/10.1021/jp510837q.
[43] M. Zhu, X. Li, W. Liu, Y. Cui, An investigation on the photoelectrochemical properties of dye-sensitized solar cells based on graphene–TiO2 composite photoanodes, J. Power Sources 262 (2014) 349–355, https://doi.org/10.1016/j.jpowsour.2014.04.001.
[44] L. Bertoluzzi, J. Bisquert, Equivalent circuit of electrons and holes in thin semiconductor films for photoelectrochemical water splitting applications, J. Phys. Chem. Lett. 3 (17) (2012) 2517–2522, https://doi.org/10.1021/jz3010909.
[45] P. Rodenas, T. Song, P. Sudhagar, G. Marzari, H. Han, L. Badia-Bou, S. Gimenez, F. Fabregat-Santiago, I. Mora-Sero, J. Bisquert, U. Paik, Y.S. Kang, Quantum dot based heterostructures for unassisted photoelectrochemical hydrogen generation, Adv. Energy Mater. 3 (2) (2013) 176–182, https://doi.org/10.1002/aenm.201200255.
[46] T. Stergiopoulos, A.G. Kontos, V. Likodimos, D. Perganti, P. Falaras, Solvent effects at the photoelectrode/electrolyte interface of a DSC: A combined spectroscopic and photoelectrochemical study, J. Phys. Chem. C 115 (20) (2011) 10236–10244, https://doi.org/10.1021/jp2007864.
[47] J. Panigrahi, Vandana, Singh R. Batra N. Gope J. Sharma M. Pathi P. Srivastava S. K. Rauthan C.M.S. Singh P.K., Impedance spectroscopy of crystalline silicon solar cell: Observation of negative capacitance, Sol. Energy 136 (2016) 412–420, https://doi.org/10.1016/j.solener.2016.06.041.
[48] Z. Ni, C. Bao, Y. Liu, Q. Jiang, W.-Q. Wu, S. Chen, X. Dai, B. Chen, B. Hartweg, Z. Yu, Z. Holman, J. Huang, Resolving spatial and energetic distributions of trap states in metal halide perovskite solar cells, Science 367 (6484) (2020) 1352–1358, https://doi.org/10.1126/science.aba0893.
[49] S. Ravishankar, T. Unold, T. Kirchartz, Comment on "resolving spatial and energetic distributions of trap states in metal halide perovskite solar cells", Science 371 (6532) (2021) eabd8014, https://doi.org/10.1126/science.abd8014.
[50] L. Xiao, Y. Yu, E.L. Schultz, E.A. Stach, T.E. Mallouk, Electron transport in dye-sensitized TiO_2 Nanowire arrays in contact with aqueous electrolytes, J. Phys. Chem. C 124 (40) (2020) 22003–22010, https://doi.org/10.1021/acs.jpcc.0c07036.
[51] J. van de Lagemaat, A.J. Frank, Effect of the surface-state distribution on electron transport in dye-sensitized TiO_2 solar cells: Nonlinear electron-transport kinetics, J. Phys. Chem. B 104 (18) (2000) 4292–4294, https://doi.org/10.1021/jp000836o.
[52] M. Antuch, P. Millet, A. Iwase, A. Kudo, The role of surface states during photocurrent switching: intensity modulated photocurrent spectroscopy analysis of BiVO4 photoelectrodes, Appl Catal B 237 (2018) 401–408, https://doi.org/10.1016/j.apcatb.2018.05.011.
[53] K.G. Upul Wijayantha, S. Saremi-Yarahmadi, L.M. Peter, Kinetics of oxygen evolution at α-Fe2O3 photoanodes: A study by photoelectrochemical impedance spectroscopy, Phys. Chem. Chem. Phys. 13 (12) (2011) 5264, https://doi.org/10.1039/c0cp02408b.
[54] B. Klahr, S. Gimenez, F. Fabregat-Santiago, T. Hamann, J. Bisquert, Water oxidation at hematite photoelectrodes: The role of surface states, J. Am. Chem. Soc. 134 (9) (2012) 4294–4302, https://doi.org/10.1021/ja210755h.
[55] C.J. Pereyra, Y. Di Iorio, M. Berruet, M. Vazquez, R.E. Marotti, Carrier recombination and transport dynamics in superstrate solar cells analyzed by modeling the intensity modulated photoresponses, Phys. Chem. Chem. Phys. 21 (36) (2019) 20360–20371, https://doi.org/10.1039/C9CP04256C.
[56] E.M. Hutter, T.J. Savenije, Thermally activated second-order recombination hints toward indirect recombination in fully inorganic $CsPbI_3$ perovskites, ACS Energy Lett. 3 (9) (2018) 2068–2069, https://doi.org/10.1021/acsenergylett.8b01106.
[57] D.R.B. Amorim, D.J. Coutinho, P.B. Miranda, R.M. Faria, Analytical model for photocurrent in organic solar cells as a function of the charge-transport figure of merit including second-order recombination, Phys. Rev. Applied 14 (3) (2020) 034046, https://doi.org/10.1103/PhysRevApplied.14.034046.
[58] C.M. Wolff, S.A. Bourelle, L.Q. Phuong, J. Kurpiers, S. Feldmann, P. Caprioglio, J. A. Marquez, J. Wolansky, T. Unold, M. Stolterfoht, S. Shoaee, F. Deschler, D. Neher, Orders of recombination in complete perovskite solar cells – Linking time-resolved and steady-state measurements, Adv. Energy Mater. 11 (45) (2021) 2101823, https://doi.org/10.1002/aenm.202101823.
[59] A.O. Alvarez, S. Ravishankar, F. Fabregat-Santiago, Combining modulated techniques for the analysis of photosensitive devices, Small Methods 5 (10) (2021) 2100661, https://doi.org/10.1002/smtd.202100661.
[60] O. Almora, D. Miravet, G.J. Matt, G. Garcia-Belmonte, C.J. Brabec, Analytical model for light modulating impedance spectroscopy (LIMIS) in all-solid-state p-n junction solar cells at open-circuit, Appl. Phys. Lett. 116 (1) (2020) 013901, https://doi.org/10.1063/1.5139571.
[61] O. Almora, Y. Zhao, X. Du, T. Heumueller, G.J. Matt, G. Garcia-Belmonte, C. J. Brabec, Light intensity modulated impedance spectroscopy (LIMIS) in all-solid-state solar cells at open-circuit, Nano Energy 75 (2020) 104982, https://doi.org/10.1016/j.nanoen.2020.104982.
[62] H. Nojima, T. Kobayashi, T. Nagase, H. Naito, Modulated photocurrent spectroscopy for determination of electron and hole mobilities in working organic solar cells, Sci Rep 9 (1) (2019) 20346, https://doi.org/10.1038/s41598-019-56945-3.
[63] H. Cachet, E.M.M. Sutter, Kinetics of water oxidation at TiO_2 nanotube arrays at different ph domains investigated by electrochemical and light-modulated impedance spectroscopy, J. Phys. Chem. C 119 (45) (2015) 25548–25558, https://doi.org/10.1021/acs.jpcc.5b06103.